

Alternative local melting-solidification of suspended nanoparticles for heterostructure formation enabled by pulsed laser irradiation

Mohammad Sadegh Shakeri^{1,}, Zaneta Swiatkowska-Warkocka¹, Oliwia Polit¹, Tatiana Itina², Alexey Maximenko³, Joanna Depciuch¹, Jacek Gurgul⁴, Marzena Mitura-Nowak¹, Marcin Perzanowski¹, Andrzej Dziedzic⁵, Jarosław Nęcki⁶*

1. Institute of Nuclear Physics Polish Academy of Sciences, PL-31342 Krakow, Poland
2. Laboratoire Hubert Curien, Université Jean Monnet, Saint-Etienne, France
3. SOLARIS NSRC, Jagiellonian University, Czerwone Maki 98, Krakow, Poland
4. Jerzy Haber Institute of Catalysis and Surface Chemistry, Polish Academy of Sciences, Niezapominajek 8, 30-239 Krakow, Poland
5. University of Rzeszów, 35-959 Rzeszów, Poland
6. University of Science and Technology, Al. Adama Mickiewicza 30, 30-059 Kraków, Poland

* Corresponding Author,

Mohammad Sadegh Shakeri (M.S. Shakeri)

Email: ms.shakeri@ifj.edu.pl

Phone No.: +48 515019092

Table of contents

a. Sample coding	3
b. Phase diagrams and temperature calculations	4
c. XPS analysis	9
d. XAS analysis	14
e. Reactive Bond Molecular dynamics simulations	18
f. DFT calculations	28
g. Raman spectra	30
h. HRTEM analysis	31
i. Zeta potential and particle size distribution	37
j. Mathematical modeling of Particle growth	38
i.1. Suspension categorization	38
i.2. Probability of probe.....	39
i.3. Particle growth without phase transition	40
i.4. Particle growth with phase transition	42
i.5. Agglomeration distribution effect	43
i.6. Application of model for the current study	43
k. The role of laser-suspension parameters	46
l. Electrocatalysis behavior	47
References	50

a. Sample coding

The samples consist of nanoparticles (Cu or CuO) suspended in a solvent (ethanol) and irradiated with different laser fluences. Here, the samples are coded according to their suspended nanoparticles and the laser fluence used for their irradiation. Accordingly, there are two groups of Cu-ethanol and CuO-ethanol samples, each irradiated with 4 different laser fluences.

It is worth noting that there is a direct correlation between the maximum temperature of the particles and the level of laser fluence. Thus, at high laser fluences, collapse of the suspension occurs due to the rapid evaporation of the particles. Here, we chose the laser fluence for each group of samples according to the heat capacity of the nanoparticles to avoid collapse of the suspension. Table S1 shows the samples synthesized and used in this manuscript.

Table S1. Coding of the synthesized samples according to the characteristics of the PLIS process

No.	Sample code	Group	Laser fluence (mJ/cm ² .pulse)	Solvent	Irradiation time (min)		
1	Cu50	Cu-ethanol	50	ethanol	60		
2	Cu100		100				
3	Cu150		150				
4	Cu200		200				
5	CuO100	CuO-ethanol	100			ethanol	60
6	CuO200		200				
7	CuO300		300				
8	CuO400		400				

b. Phase diagrams and temperature calculations

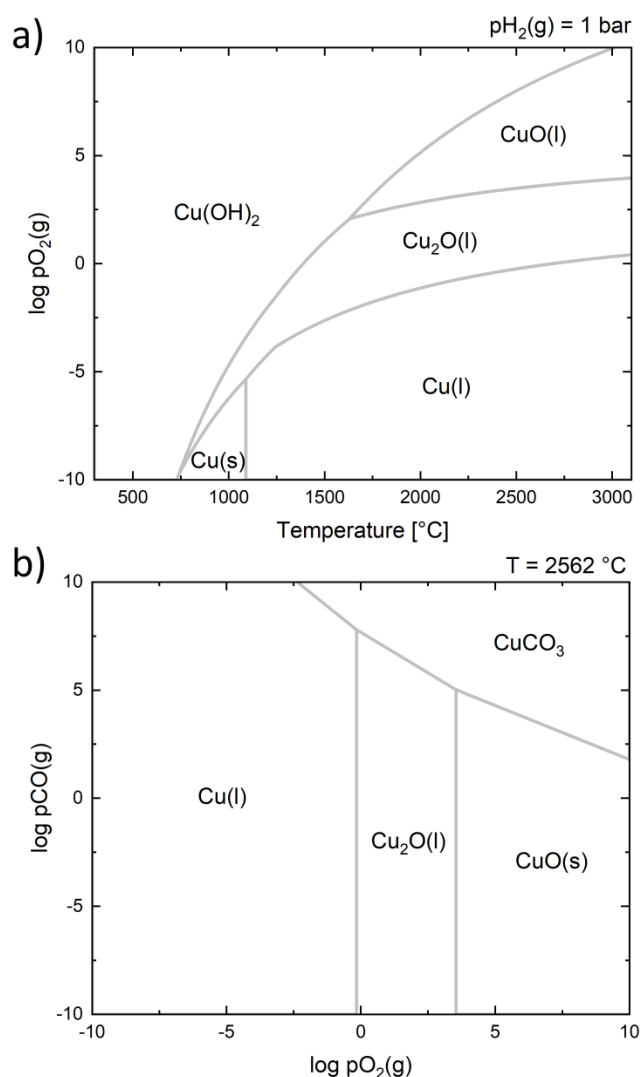


Fig. S1. Stability diagrams of Cu-O-C-H system calculated using HSC Chemistry software. (a) $\log P_{O_2} - T$ diagram at constant $P_{H_2} = 1$ bar showing Cu, CuO, Cu₂O and Cu(OH)₂ phases and (b) $\log P_{CO} - \log P_{O_2}$ diagram at 2835° K showing Cu, CuO, Cu₂O and CuCO₃ phases. The elemental configuration for plotting these diagrams was chosen because copper, oxygen, carbon, and hydrogen are the building blocks of Cu-ethanol and CuO-ethanol suspensions subjected to thermal conditions during pulsed laser irradiation of suspension (PLIS). According to C-O-H stability diagram, there is a possibility of crystallization of copper hydroxide when the temperature is low. Moreover, Cu-O-C stability diagram shows a Cu-Cu₂O phase equilibrium line at $P_{O_2} = 1$ ($\log P_{O_2} = 0$), when the temperature is fixed at 2835° K. Higher oxygen content leads to the formation of Cu oxide (I), while Cu is stable at lower oxygen content.

Table S2. Transition temperature, enthalpy, and laser fluence required for the reaction pathways of Cu and CuO phases

No.	Heating regime	Reaction	Initial Temperature (°K)	Final Temperature (°K)	ΔH (kJ/mole)
Cu					
J1 _{Cu}	Heating of solid Cu	$\text{Cu (s)} + h\nu \rightarrow \text{Cu (s)}$	$T_0/ 298$	$T_m/ 1357$	29.642
J2 _{Cu}	Cu melting	$\text{Cu (s)} + h\nu \rightarrow \text{Cu (l)}$	$T_m/ 1357$	$T_m/ 1357$	13.264
J3 _{Cu}	Heating liquid Cu	$\text{Cu (l)} + h\nu \rightarrow \text{Cu (l)}$	$T_m/ 1357$	$T_b/ 2843$	46.636
J4 _{Cu}	Cu boiling	$\text{Cu (l)} + h\nu \rightarrow \text{Cu (g)}$	$T_b/ 2843$	$T_b/ 2843$	300.150
CuO					
J1 _{CuO}	Heating of solid CuO	$\text{CuO (s)} + h\nu \rightarrow \text{CuO (s)}$	$T_0/ 298$	$T_{\text{CuO(s)} \rightarrow \text{Cu}_2\text{O(s)}/1379}$	57.073
J2 _{CuO}	CuO decomposition to solid Cu ₂ O	$4\text{CuO (s)} + h\nu \rightarrow 2\text{Cu}_2\text{O (s)} + \text{O}_2 \text{ (g)}$	$T_{\text{CuO(s)} \rightarrow \text{Cu}_2\text{O(s)}/1379}$	$T_{\text{CuO(s)} \rightarrow \text{Cu}_2\text{O(s)}/1379}$	63.881
J3 _{CuO}	Heating of solid Cu ₂ O	$\text{Cu}_2\text{O (s)} + h\nu \rightarrow 2\text{Cu}_2\text{O (s)}$	$T_{\text{CuO(s)} \rightarrow \text{Cu}_2\text{O(s)}/1379}$	$T_m/ 1517$	12.378
J4 _{CuO}	Cu ₂ O melting	$\text{Cu}_2\text{O (s)} + h\nu \rightarrow \text{Cu}_2\text{O (l)}$	$T_m/ 1517$	$T_m/ 1517$	65.600
J5 _{CuO}	Heating of liquid Cu ₂ O	$\text{Cu}_2\text{O (l)} + h\nu \rightarrow \text{Cu}_2\text{O (l)}$	$T_m/ 1517$	$T_{\text{Cu}_2\text{O(l)} \rightarrow \text{Cu(g)}/2858}$	133.965
J6 _{CuO}	Cu ₂ O decomposition to gaseous Cu	$2\text{Cu}_2\text{O (l)} + h\nu \rightarrow 4\text{Cu (g)} + \text{O}_2 \text{ (g)}$	$T_{\text{Cu}_2\text{O(l)} \rightarrow \text{Cu(g)}/2858}$	$T_{\text{Cu}_2\text{O(l)} \rightarrow \text{Cu(g)}/2858}$	706.888

Table S3. Inherent optical and thermal properties of raw materials

	n	k	λ (nm)	ρ (g/cm ³)	K_L ((Wm ⁻² K ⁻¹))	K_V ((Wm ⁻² K ⁻¹))	Nu _d
Cu	1.1164	2.59568	532	8.96	-	-	-
CuO	2.5648	0.6222		6.31	-	-	-
Ethanol	1.3614	-		0.789	0.171	0.0253	2
Vacuum	1.0000	-		-	-	-	-

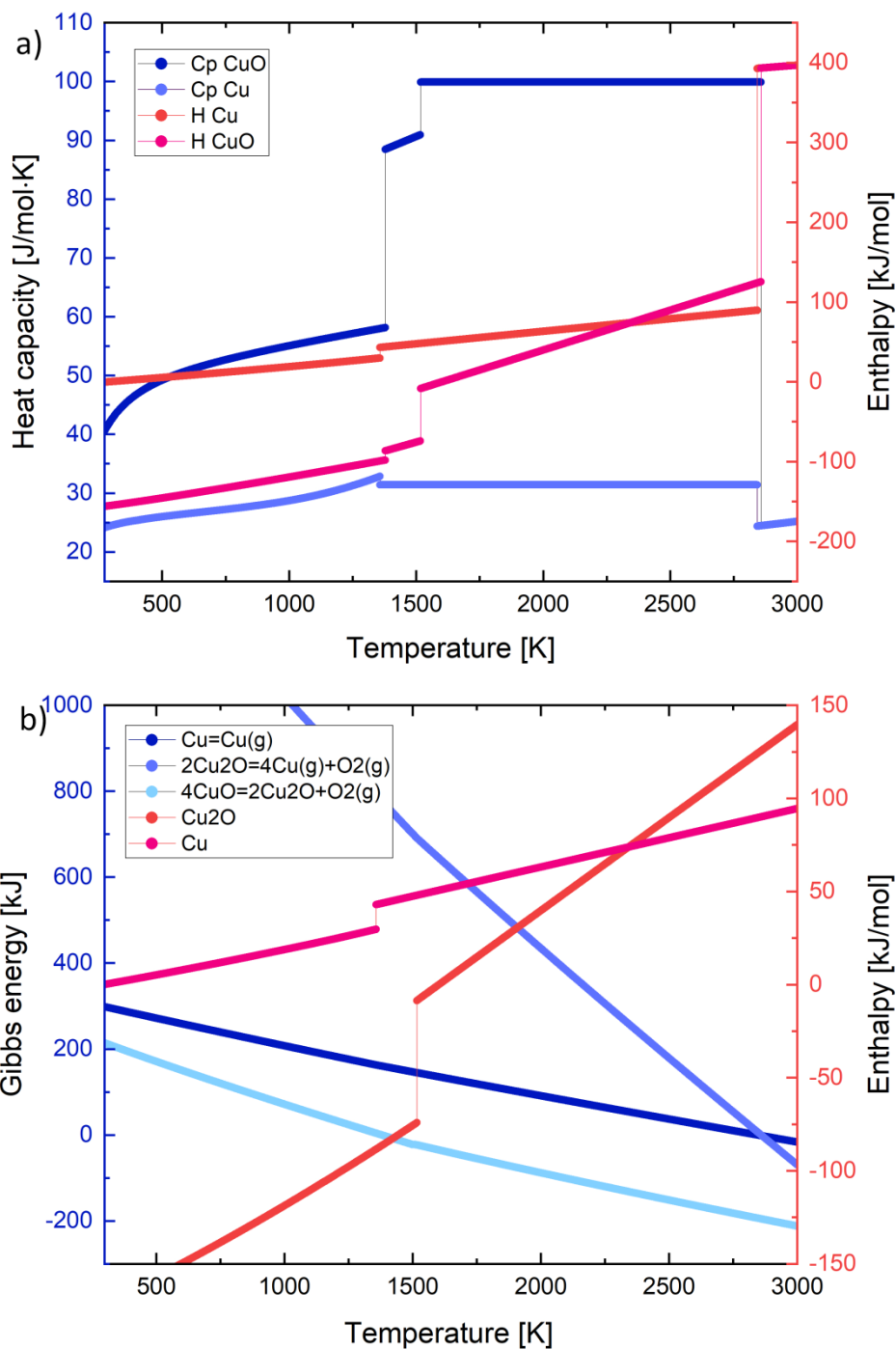


Fig. S2. (a) The enthalpy and heat capacity required to solve equation (1), and (b) the Gibbs free energy curves of reactions showing the phase transitions in the thermal paths of Cu and CuO, and the enthalpy curves of the phases apparently showing their melting temperatures. These data were calculated using HSC Chemistry software to solve equation (1) in the context of the heating-melting-evaporation model and to derive the reaction pathway in both Cu and CuO systems.

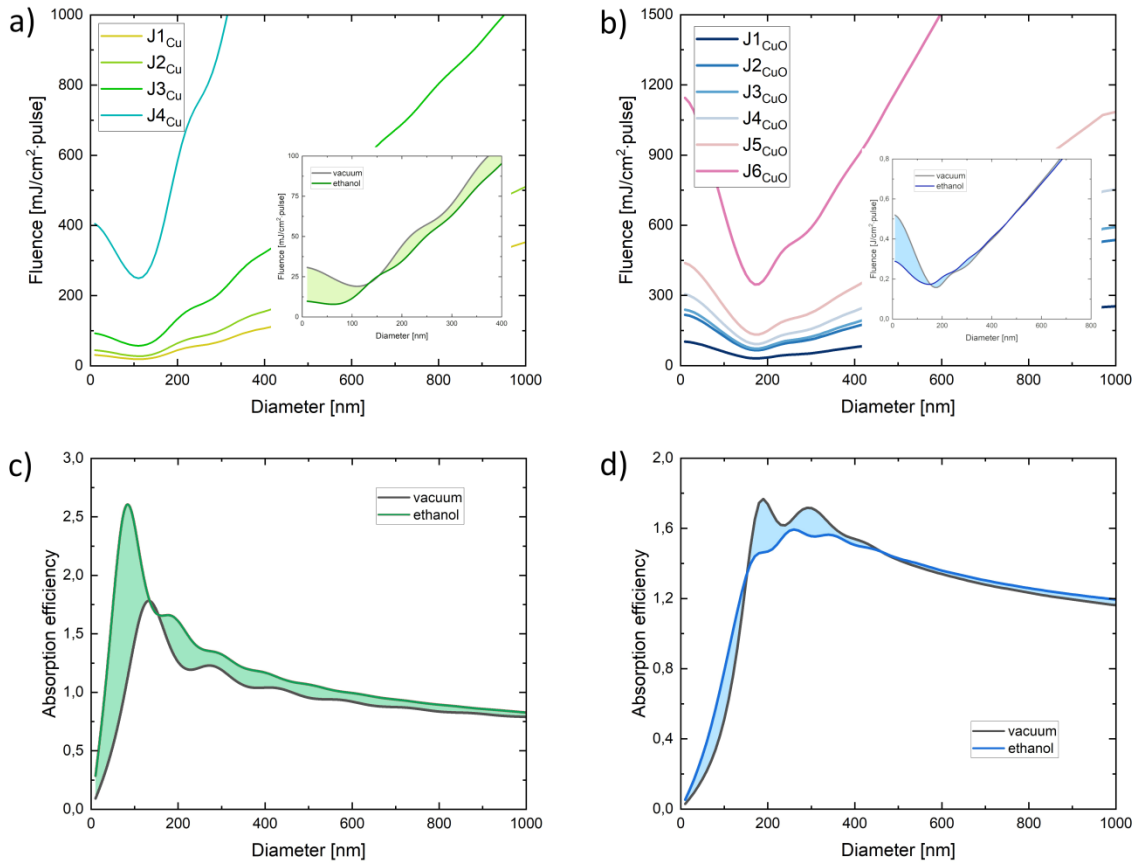


Fig. S3. J-D diagram for (a) Cu and (b) CuO in vacuum and absorption efficiency of (c) Cu and (d) CuO in ethanol and vacuum. The difference between J-D in ethanol and vacuum, illustrated by the highlighted area, is the effect of dynamic absorption efficiency on the J-D diagram. Obviously, the refractive index of the solvent, which is crucial for the calculation of the absorption cross section, changes dynamically with increasing temperature during the PLIS process [S1, S2]. At higher temperatures, the density and viscosity of the liquid decrease, so light propagates faster in the medium due to the decrease in refractive index. Thus, at higher temperatures, the refractive index of the ethanol solvent inclines to the refractive index of the vacuum [S3]. Dynamic absorption during the PLIS process is affected by the difference between the refractive indices of the particles in ethanol and in vacuum. The highlighted region between the J-D boundaries shown for the ethanol and vacuum media is the flexible boundary of the J-D phase diagram due to the dynamic nature of the refractive index.

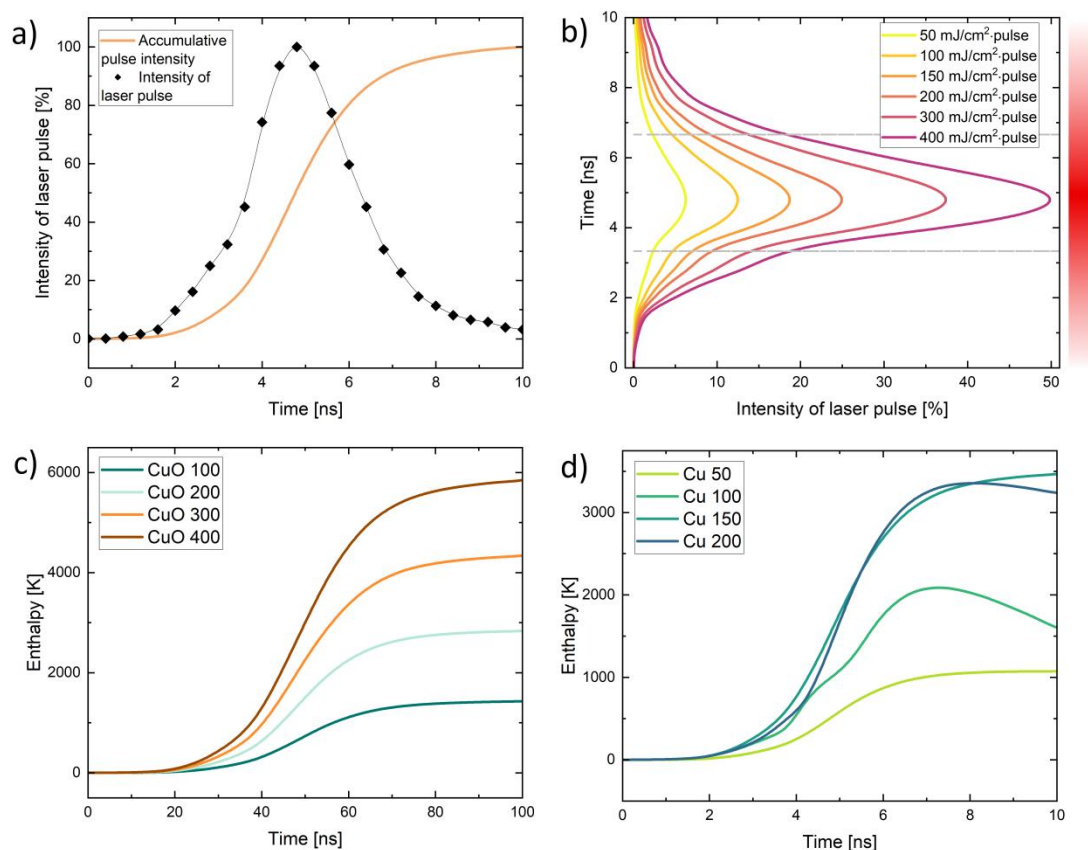


Fig. S4. (a) Pulse shape of the laser and accumulative energy of the pulse, and (b) propagation of the pulse shape in direction X. Accumulative enthalpy from absorption of a laser pulse by a 100 nm Cu sphere, (c) without and (d) with heat dissipation. The pulse shape indicates the absorption contribution in time or direction [7]. When the Gaussian pulse shape is divided into three regions, the absorption rate is considerable in the middle region, i.e., the second third. Moreover, the probability of heat release is related to the pulse shape. The insufficient time for dissipation and the high absorption rate are the reasons why we cannot see the effects of dissipation on the temperature of the particles in the first and second thirds of the pulse shape, respectively. In the last third of the pulse, there is sufficient time for dissipation of energy from the accumulated energy, which is hardly charged by the low absorption rate; therefore, heat dissipation is maximized in this part of the pulse shape. If we compare the amount of accumulated enthalpy with and without heat release, we see the decreasing trend of enthalpy accumulated in the particle in the last third of the pulse shape.

c. XPS analysis

The binding energy (BE) in the range of 925-960 eV reveals complex spectral features of the Cu 2p photoelectron spectrum (Fig. 2c,f). In addition to the well-separated spin-orbit peaks with total momentum $j = 3/2$ and $j = 1/2$, there are much weaker additional structures in between associated with shake-up satellites. It is worth noting that shake-up satellites of varying intensity can only be observed for Cu^{2+} , which has a d^9 configuration in the ground state, and they can occur when outgoing photoelectrons interact with valence electrons excited to higher energy levels. The shake-up satellites do not occur in d^{10} Cu^0 or Cu^+ spectra. Unfortunately, it is not possible to distinguish between Cu^0 and CuO , as well as between $\text{Cu}(\text{OH})_2$ and Cu_2O , because the chemical shift of the Cu $L_3M_{45}M_{45}$ band is very small.

Four doublets were used to properly fit the Cu 2p spectra (Fig. 2c,f). The spin-orbit splitting of all doublets was in the range of 19.7-19.9 eV. The most intense components come from the metallic Cu^0 and Cu_2O species (932.5-932.9 eV), octahedral CuO (933.3-934.0 eV), and Cu^{2+} hydroxide species (>935.0 eV) [14, 19-20]. The weakest doublet ($<5.6\%$) with Cu $2p_{3/2}$ BE values of 930.9-931.6 eV is caused by the different charging of the supported Cu particles compared to the silica support surface. A similar phenomenon has already been observed for metallic ruthenium on MgO and SiO_2 [S4] and for Ru/Ce systems on mesocellular silica foam [S5] and explained as a final state effect due to the higher internal conductivity of the supported Ru compared to the conductivity of the dielectric support.

The kinetic energy of the Cu $L_3M_{45}M_{45}$ Auger peaks was calculated for two main contributions marked by arrows in Fig. 2d,g. For this purpose, the data listed in Supplementary Tables S4 and S5 were used. The first contribution shows the Auger parameter of copper near 1849.1 eV, which is consistent with Cu_2O in the literature [15, 20]. The second contribution shows the Auger parameter near 1851.6 eV for all measured samples. According to Biesinger et al [13, 15], the distinction between Cu^0 (1851.2 eV for metallic Cu) and Cu^{2+} species (1851.3 eV for CuO and 1850.9 eV for $\text{Cu}(\text{OH})_2$) is almost impossible. Therefore, the second contribution should be treated as coming from metallic copper and Cu^{2+} oxide species together (and marked in this way in Fig. 2c,f).

The O 1s spectra (Fig. 2e) of Cu-ethanol samples show four components: (i) a peak at 529.9-530.7 eV related to oxygen in copper oxides (CuO and Cu_2O), (ii) a peak assigned to hydroxyl groups and $\text{Cu}(\text{OH})_2$ (BE = 531.5-531.9 eV), (iii) adsorbed water (BE = 532.6-533.7 eV), and (iv) a weak contribution at BE > 534.6 eV that can be attributed to oxygen in organic impurities [15, 19]. Exactly the same components are visible in the O 1s spectra of CuO -ethanol samples (Fig. 2h). It is worth noting that only one component corresponding to Cu^0 and Cu^{2+} species is visible in the CuLMM spectrum of the CuO -raw sample. The absence of a component corresponding to Cu^+ species is reflected in the O 1s spectrum as a shift of the component with BE = 529.9 eV to lower values of

binding energy compared to the other samples (530.6-531.0 eV). The shift to lower BE values of the component corresponding to Cu_2O and CuO is also evident in the $\text{Cu}50$ spectrum.

Several contributions were found in the C 1s core lines of the studied samples (Fig. S5 and Table S6). The organic contaminants (285.0 eV), C-O groups (285.9-286.6 eV), and C=O groups (287.9-288.8 eV) were the components with the highest contribution to each spectrum. In addition, a small amount of carbides and a significant amount of O-C=O groups (289.1-290.0 eV) were found. The hydrocarbon impurities were used as internal calibration for our samples, as mentioned above.

Finally, the quantitative information presented here should be treated with some caution, as it has been previously shown that nanoparticle dispersion can affect the observed spectral intensities [21], and particle size could also affect the intensities of shake-up lines in Cu 2p spectra [22].

Table S4. The BE values (eV) and relative areas of the components (%) of Cu 2p_{3/2}, Cu LMM, and O 1s peaks for Cu-ethanol samples

Core excitation	Doublet No.	Cu50		Cu100		Cu150		Cu200	
		BE (eV)	Area (%)	BE (eV)	Area (%)	BE (eV)	Area (%)	BE (eV)	Area (%)
Cu 2p _{3/2}	1	931.2	4.0	931.3	4.9	931.2	4.7	931.2	3.5
	2	932.5	42.3	932.6	63.2	932.6	70.9	932.6	52.1
	3	933.4	33.3	933.3	23.5	933.6	18.3	933.4	27.3
	4	935.0	20.4	935.4	8.4	936.3	6.1	935.2	17.1
Cu LMM	1	568.3	32.2	568.2	27.7	567.9	20.6	568.3	42.0
	2	569.7	67.8	570.2	72.3	570.1	79.4	570.1	58.0
O 1s	1	529.9	50.1	530.6	36.0	530.6	32.2	530.7	20.5
	2	531.5	36.9	531.9	5.5	531.8	18.7	531.9	51.3
	3	533.7	11.0	533.0	55.6	532.6	44.9	532.8	24.0
	4	535.1	2.0	535.4	2.9	535.1	4.2	534.6	4.2

Table S5. The BE values (eV) and relative areas of the components (%) of Cu 2p_{3/2}, Cu LMM, and O 1s peaks for CuO-ethanol samples

Core excitation	Doublet No.	CuO-raw		CuO100		CuO200		CuO300		CuO400	
		BE (eV)	Area (%)	BE (eV)	Area (%)	BE (eV)	Area (%)	BE (eV)	Area (%)	BE (eV)	Area (%)
Cu 2p _{3/2}	1	930.9	1.0	931.6	5.6	931.4	5.3	931.3	3.4	931.5	4.5
	2	932.8	33.8	932.9	43.2	932.8	57.6	932.8	49.9	932.9	59.7
	3	934.0	44.9	933.7	36.0	933.4	25.3	933.6	25.4	933.5	23.9
	4	935.6	20.3	935.7	15.2	935.3	11.8	935.2	21.3	935.1	11.9
Cu LMM	1	568.9	100	568.7	41.4	568.4	35.6	568.3	30.7	568.2	23.6
	2	--	--	570.3	58.6	570.3	64.4	570.2	69.3	570.3	76.4
O 1s	1	529.9	45.2	530.6	47.8	530.8	45.0	530.9	28.4	531.0	32.9
	2	531.5	18.1	532.1	33.3	532.1	26.4	532.1	39.8	532.1	37.8
	3	533.0	32.9	533.7	15.3	533.2	22.1	533.3	26.7	533.3	20.6
	4	534.8	3.8	535.2	3.6	535.7	6.5	535.8	5.1	535.7	8.7

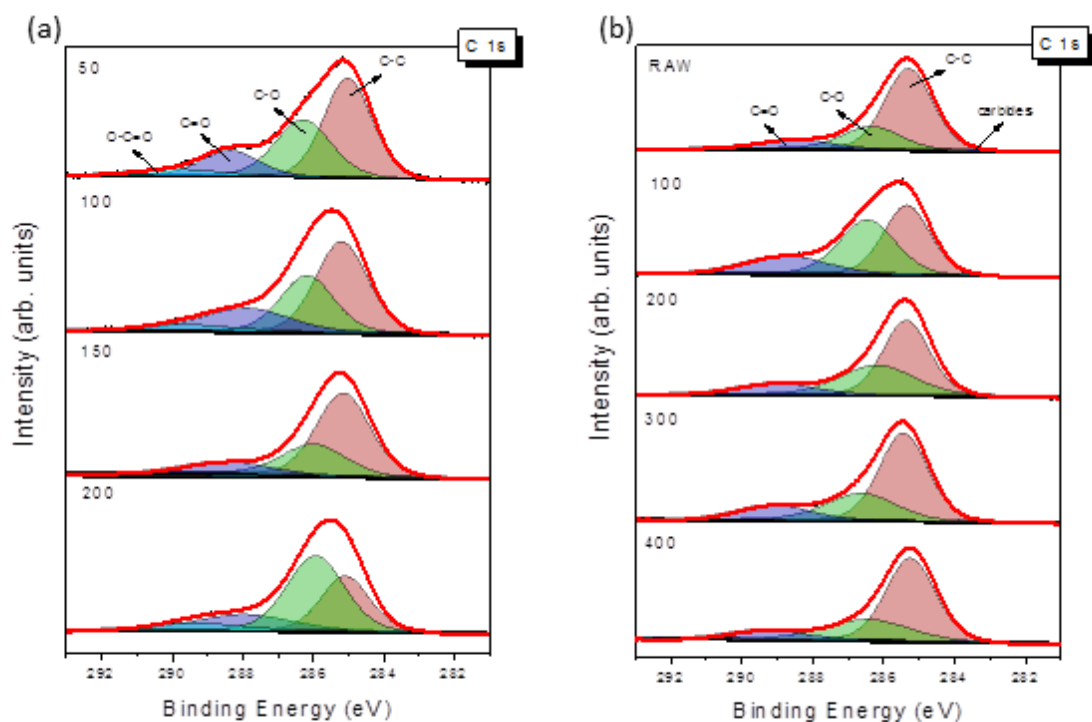


Fig. S5. C 1s XPS spectra of (a) Cu-ethanol and (b) CuO-ethanol samples

Table S6. The BE values (eV) and relative areas of the components (%) of C 1s core excitation for Cu-ethanol and CuO-ethanol samples

Sample	carbides		C-C, C-R		C-OR		C=O		O-C=O	
	BE (eV)	Area (%)	BE (eV)	Area (%)	BE (eV)	Area (%)	BE (eV)	Area (%)	BE (eV)	Area (%)
Cu50	---		285.0	48.2	286.2	31.9	288.3	14.3	290.0	5.6
Cu100	---		285.1	46.9	286.1	29.8	287.9	18.9	289.7	4.4
Cu150	282.9	0.8	285.1	60.0	285.9	26.3	288.5	12.9	---	
Cu200	283.0	0.4	285.0	29.8	285.9	48.3	287.9	15.7	289.4	5.8
CuO-raw	283.7	1.7	285.2	65.6	286.3	22.0	288.5	10.7	---	
CuO100	283.4	0.4	285.3	41.8	286.4	39.0	288.8	18.8	---	
CuO200	---		285.3	54.0	286.1	33.2	---		289.1	12.8
CuO300	283.3	0.8	285.4	59.6	286.6	25.3	---		289.1	14.3
CuO400	283.0	0.6	285.2	63.3	286.4	25.8	---		289.4	10.3

d. XAS analysis

Table S7. The detected absorptions in Cu K-edge of different samples

Absorption energy (eV)	Pre-edge	Excrescence	Peak
Cu50	8980.2	8991.9	8996.5
Cu100	8980.8	8991.9	8995.8
Cu200	8981.4	8991.9	8994.5
CuO100	8984.3	8992.7	8996.7
CuO200	8984.1	8992.7	8996.6
CuO400	8981.3	8992.7	8994.9

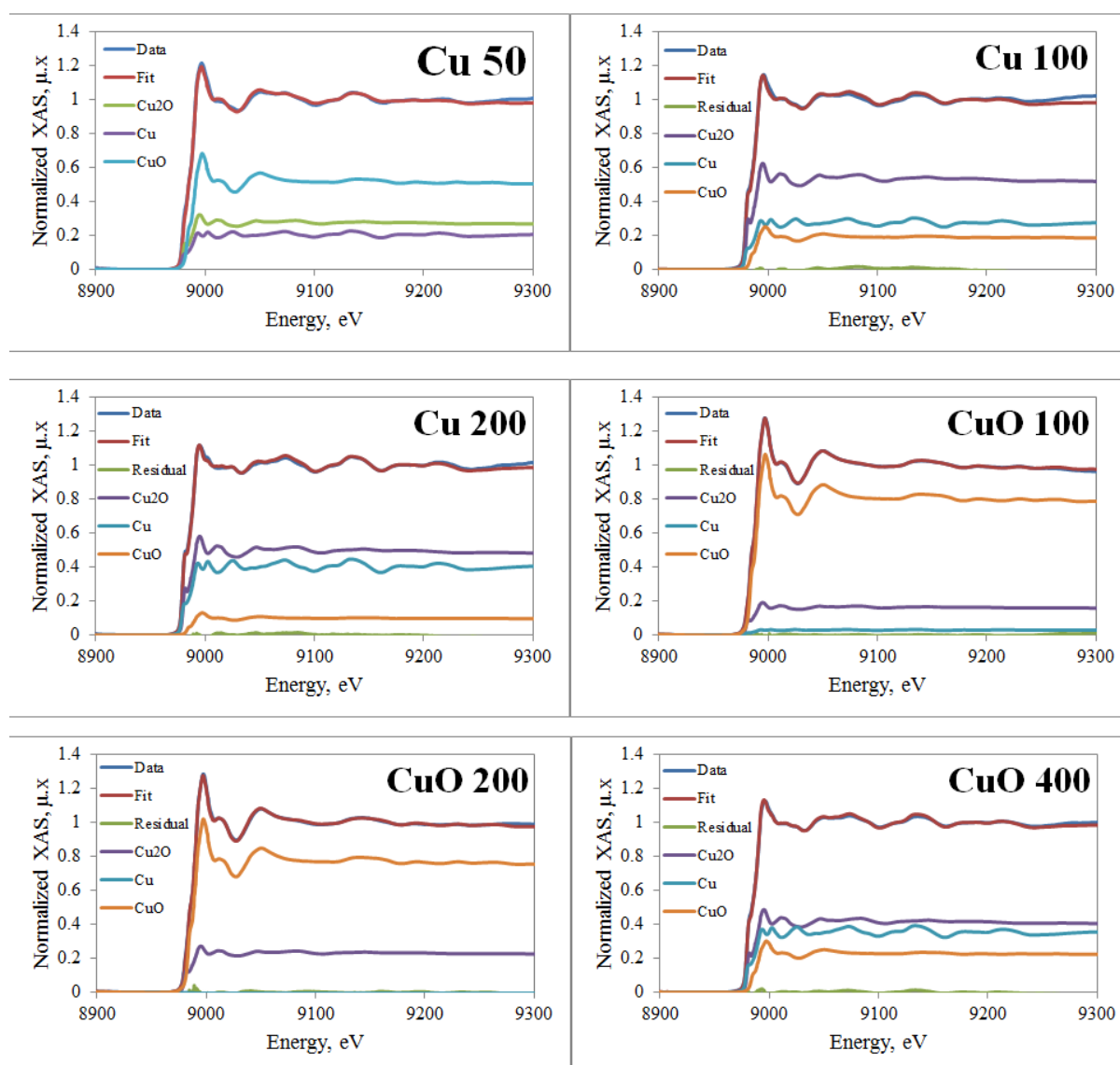


Fig. S6. Linear combination fitting (LCF) of normalized EXAFS spectra of (a) Cu50, (b) Cu100, (c) Cu200, (d) CuO100, (e) CuO200, and (f) CuO400 samples using copper foil, CuO Merck, and Cu₂O Merck references.

Table S8. Quantitative phase analysis of samples derived from LCF of EXAFS spectra

	Cu	CuO	Cu ₂ O
Cu-50	20.6	51.8	27.6
Cu-100	27.5	19.2	53.3
Cu-200	40.4	10.0	49.6
CuO-100	3.1	80.6	16.3
CuO-200	0	77.3	23.2
CuO-400	35.5	22.9	41.6

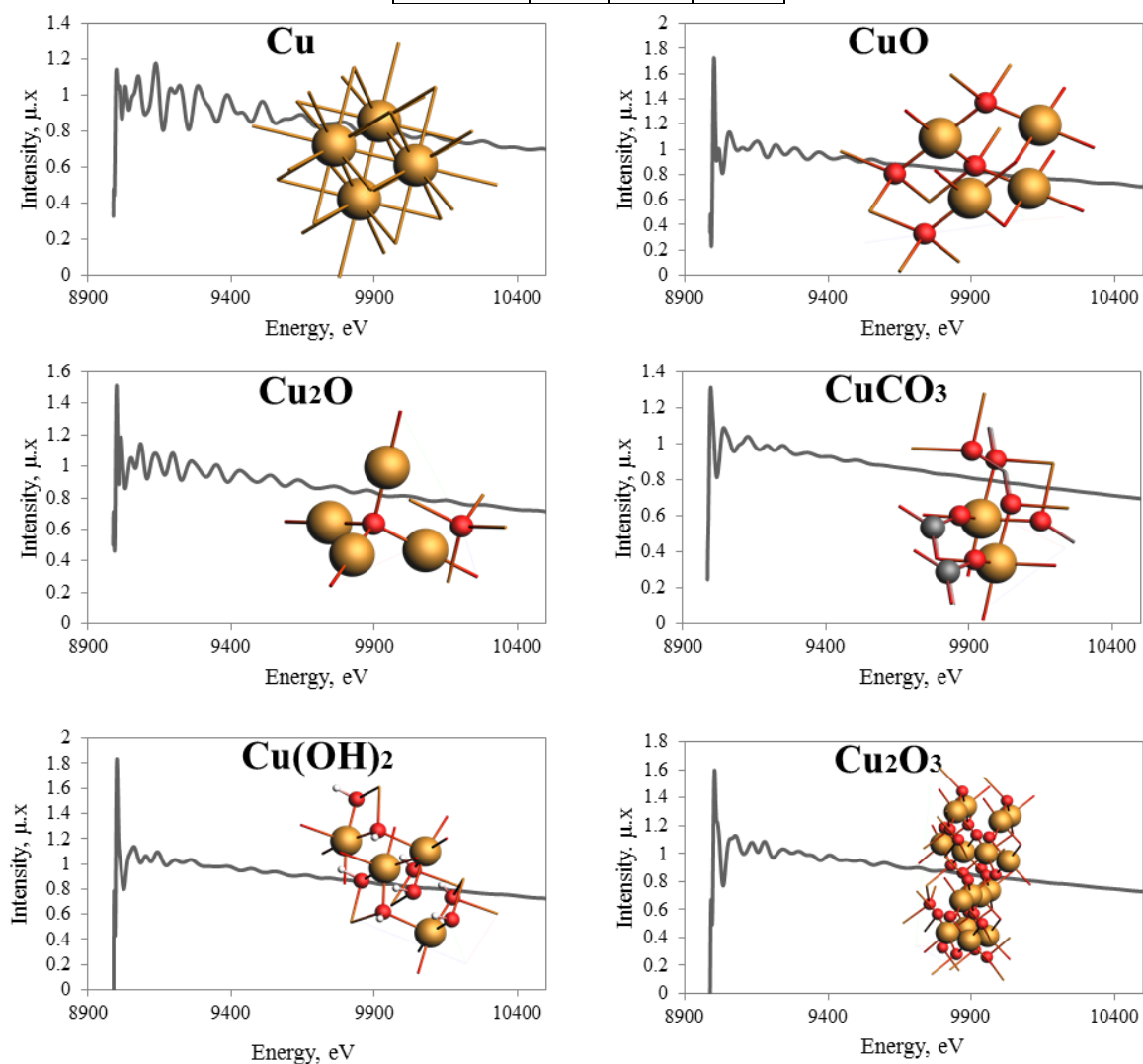


Fig. S7. Calculated EXAFS spectra of copper compounds that can be thermodynamically or kinetically crystallized during the PLIS process. The spectra were calculated using the jfeff10 software. For the calculation of Cu K-edge, we used the parameters, RPATH: 5.5, SCF: 10, Exchange: Dirac-Hara+HL and FMS: 25. These parameters were set to obtain the best correlation between calculated and measured spectra. CuCO₃, Cu(OH)₂ and Cu₂O₃ models without measured references were calculated with the same set of parameters. The yellow, red, black and white colors in the atomic models represent Cu, O, C and H atoms, respectively.

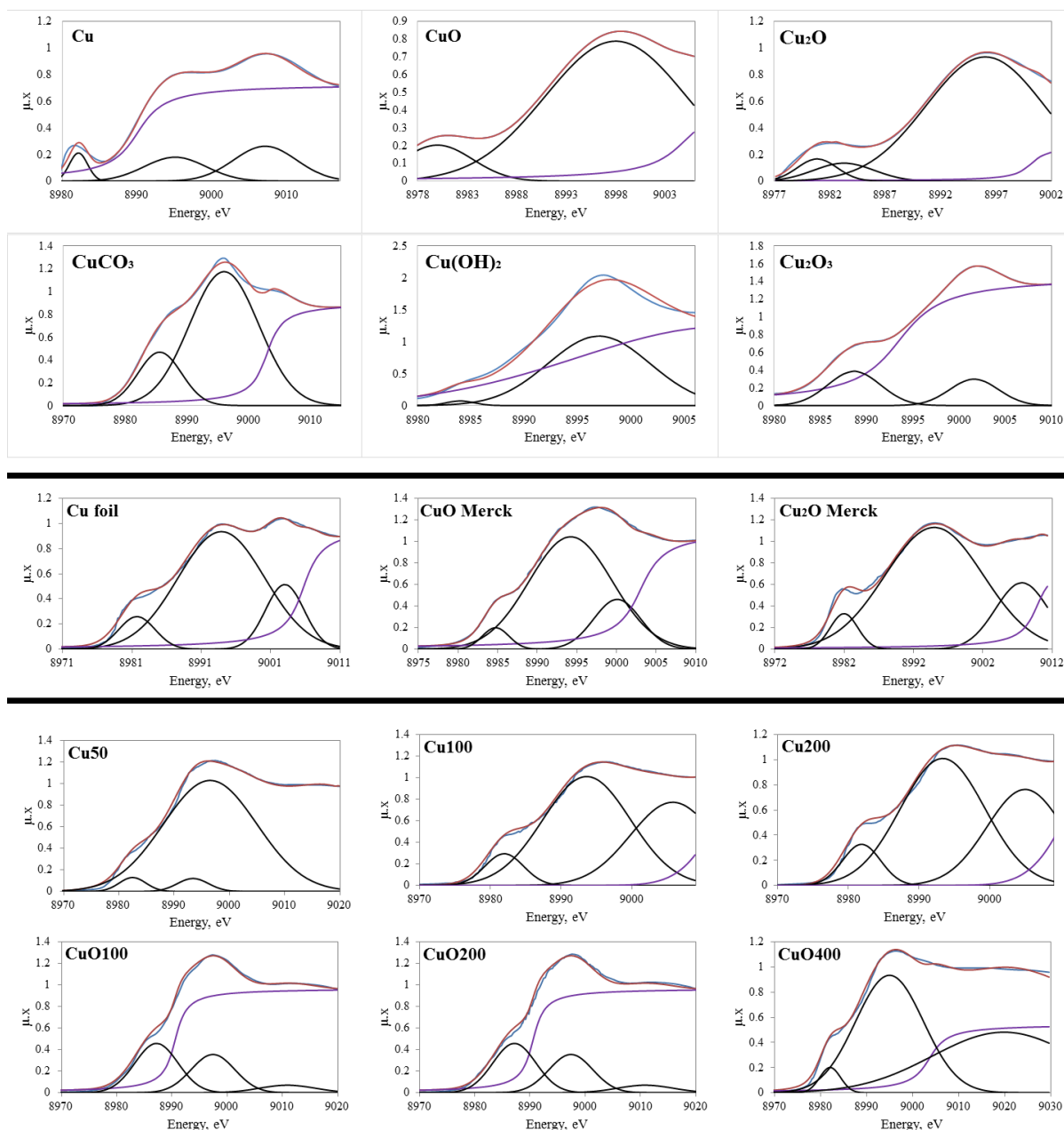


Fig. S8. Gaussian fitting of XANES spectra of calculated Cu, CuO, Cu₂O, CuCO₃, Cu(OH)₂, and Cu₂O₃, measured references of Cu foil, CuO Merck, and Cu₂O Merck, and also measured samples of Cu50, Cu100, Cu200, CuO100, CuO200, and CuO400. In all spectra, the blue, red, black, and purple curves are the illustrations of the XANES data, the fitted curve, the Gaussian doublet, and arc tangent step, respectively. After obtaining an incredibly convincing LCF result, we attempted to calculate the XAS spectra of all possible crystallized phases in our system. Even though a number of these phases crystallize only to a small extent, they affect the final properties of the composite powder. The number of Gaussian doublets is considered as the total number of pre-edges, peaks, and possible excrescences in each spectrum. Also, an arc tangent step is added to achieve an adequate fit. In the case of an unsuitable fitting result, a doublet is removed or added to balance the fitting results.

Table S9. Peak positions of XANES spectra of calculated references, measured references, and samples. Here we report the position of the peaks and also the position of the peaks resulting from the Gaussian fit of the XANES spectra of all calculated and measured samples. The agreement between the calculated models and the measured samples is obvious for the Cu, CuO, and Cu₂O spectra. Due to the proximity of the absorption peaks, an accurate separation between the phases to predict the content of the sample is not possible. Incidentally, these results can be used as a reference for work related to copper oxidation.

		Peaks on the curve			Gaussian fitted peaks		
Calculated references	Cu(OH) ₂	8983.86	8997.45	-	8984.59	8997.45	-
	Cu ₂ O ₃	8988.82	9001.49	-	8988.48	9001.49	-
	Cu ₂ O	8981.35	8995.59	-	8980.59	8984.09	8996.44
	CuCO ₃	8986.94	8995.01	9004.02	8984.53	8995.01	-
	CuO	8980.50	8998.11	-	8979.50	8997.22	-
	Cu	8981.28	8995.42	9007.19	8982.16	8993.90	9006.17
references	Cu ₂ O	8981.70	8994.60	-	8981.49	8994.60	9007.58
	Cu	8980.83	8993.51	9001.64	8981.21	8993.30	9002.16
	CuO	8984.84	8996.34	-	8983.94	8993.34	9000.83
Samples	Cu-50	8981.09	8992.62	8996.47	8981.65	8992.62	8995.57
	Cu-100	8981.47	8995.74	-	8981.09	8992.88	9005.25
	Cu-200	8981.47	8994.37	-	8981.30	8992.83	9004.44
	CuO-100	8985.19	8996.73	-	8986.72	8996.73	9010.66
	CuO-200	8985.87	8996.17	9011.61	8985.87	8995.53	9008.73
	CuO-400	8981.69	8994.97	9015.65	8981.47	8994.37	9018.70

e. Reactive Bond Molecular dynamics simulations

Table S10. Results of gas chromatographic analyzes of Cu-ethanol and CuO-ethanol samples before and after irradiation with different laser fluences. The formation of C₂H₄ and C₂H₆ and the increase in the content of CH₄ and CO show the partial dissociation of the solvent during the PLIS process.

Gas	Unit	Before irradiation		After irradiation			
		Cu-ethanol	CuO-ethanol	Cu100	Cu200	CuO200	CuO400
CO ₂	PPM	704.3	705.4	674.8	641.5	762.8	845.5
CO	PPM	1.9	1.9	10.4	14.8	29.5	208.9
O ₂	%	20.68	20.70	20.71	20.69	20.61	20.47
CH ₄	PPM	2.9	2.6	3.1	3.7	7.8	35.8
C ₂ H ₆	PPM	0.0	0.0	0.8	2.7	2.6	14.7
C ₂ H ₄	PPM	0.0	0.0	0.0	7.3	1.3	67.5

Table S11. Details of the simulation models, temperature regime, and timing of modeling for the molecular dynamics simulations with reactive bonds performed in this study

Code	Explanation	Number of Cu atoms	Number of oxygen atoms	Number of solvent molecules	Maximum temperature of solid phase (°K)	Maximum temperature of solvent (°K)	Simulation box size (Å)	Size of solid phase	Time (ps)
MB1	Cu sphere-ethanol	5473	-	3000	2843		100*100*100	5 nm sphere	250
MB2	CuO sphere-ethanol	2927	2940	3000	2858		100*100*100	5 nm sphere	250
MB3	Cu sphere-ethanol	5473	-	1500	1500		70*70*70	5 nm sphere	125
MB4	Cu sphere-ethanol	5473	-	1500	1000		70*70*70	5 nm sphere	125
MB5	Cu sphere-ethanol	5473	-	1500	2843	1500	70*70*70	5 nm sphere	125
MB6	Cu sphere-ethanol	5473	-	1500	2843	298	70*70*70	5 nm sphere	125
MB7	Cu (111) slab-ethanol	400	-	450	2843		25.52*22.11*100	4 layers slab	250
MB8	CuO (111) slab-ethanol	200	200	300	2858		14.69*30.06*100	4 layers slab	250
MB9	Cu sphere-Cu sphere-ethanol	2410	-	1000	2843		50*50*100	Double 3 nm spheres	125
MB10	Cu-sphere-ethanol	5473	-	1500	2843		70*70*70	5nm sphere	125
				1000	2000		80*80*80		125
				1000	1500		90*90*90		125
MB11	CuO-sphere-ethanol	2927	2940	1500	2858		70*70*70	5 nm sphere	125
				1000	2000		80*80*80		125
				1000	1500		90*90*90		125

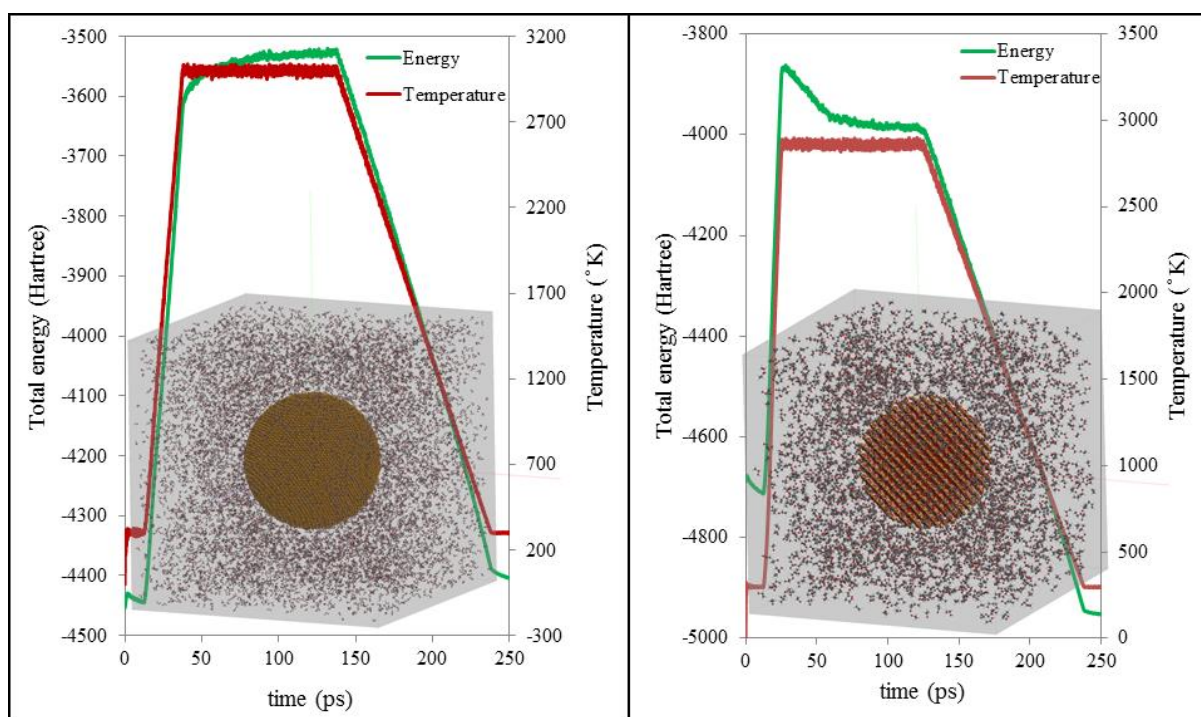


Fig. S9. Temperature regime, total energy, and modeling box of (a) Cu-ethanol (MB1) and (b) Cu-ethanol (MB2) models

Table S12. First appearance and beginning of the increase in the content of molecules produced by the decomposition of ethanol. There are also other molecules formed by the dissociation of ethanol; by the way, we have indicated only the molecules with an atomic percentage higher than 1%.

No	Molecule	First appearance		Beginning of the increase in the content	
		Cu sphere-ethanol	CuO sphere-ethanol	Cu sphere-ethanol	CuO sphere-ethanol
1	H ₂ O	27.125	15.975	27.125	15.975
2	C ₂ H ₄	25.925	16.400	27.125	16.400
3	C ₂ H ₅	14.65	18.900	20.125	18.900
4	C ₂ H ₃	32.225	19.325	32.225	22.600
5	CH ₃	23.5	15.775	36.725	21.250
6	C ₂ H ₂	36.325	20.500	37.45	20.500
7	C ₂	49.9	31.025	52.025	32.000
8	H	25.7	6.000	29.975	21.900
9	CO	35.725	24.825	35.725	24.825
10	H ₂	34.775	23.425	34.775	23.425
11	C ₂ H ₅ O	-	0.850	-	0.850
12	C ₂ H ₄ O	-	1.200	-	1.200
13	C ₂ H ₂ O	-	5.875	-	5.875

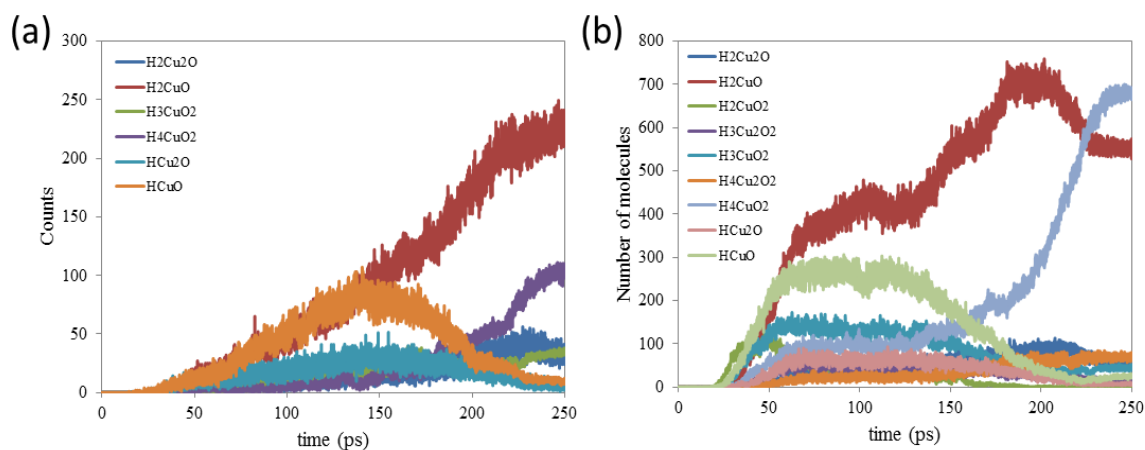


Fig.S10. Formation of oxygenated copper compounds during RBF-MD simulations of (a) Cu-ethanol (MB1), (b) CuO-ethanol (MB2) models. There are also other molecules that form between Cu and O atoms; incidentally, we have listed here only those with atomic percentages greater than 1%. Most of the oxygenated copper compounds reported here are formed as a result of surface oxidation of copper by absorption of OH and H₂O groups.

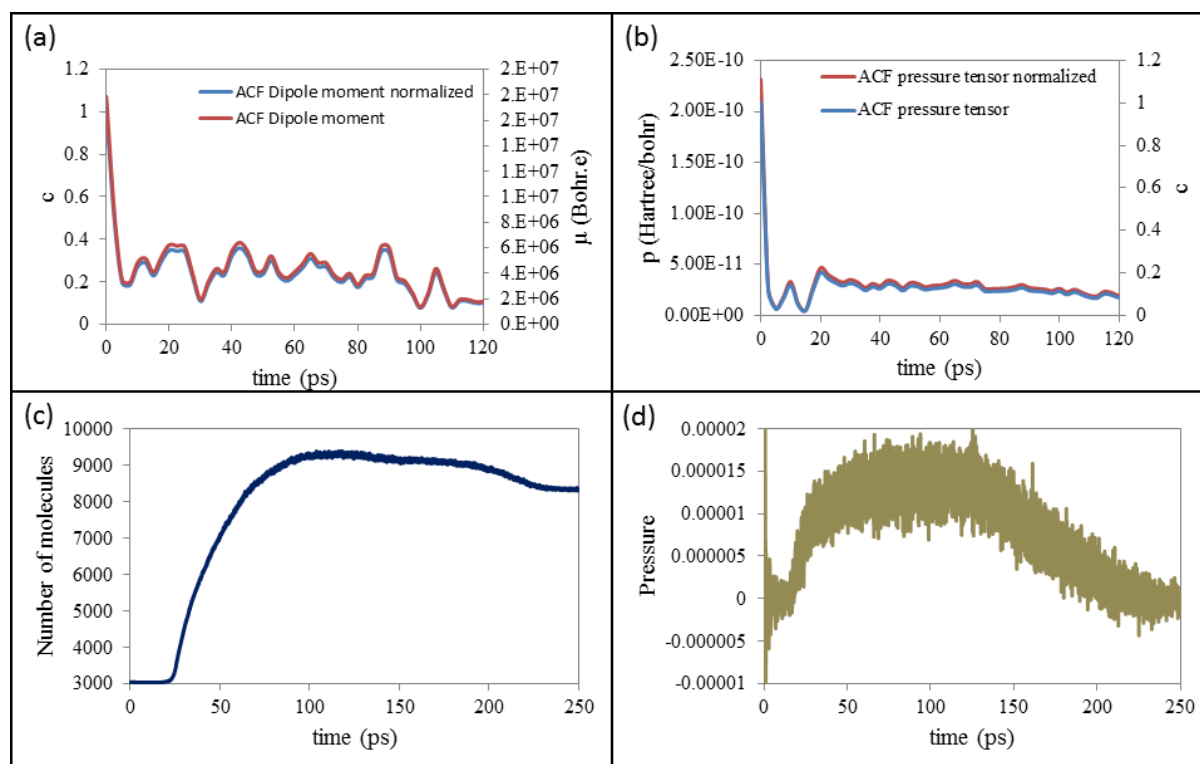


Fig. S11. (a) Pressure tensor and (b) dipole moment, autocorrelated functions of the Cu-Sphere (MB1) model. Suitable correlations are observed for both the pressure tensor and the dipole moment. (c) Number of molecules and (d) pressure change within the same simulation box at different time steps. The internal pressure has a direct functionality with the number of molecules during heating.

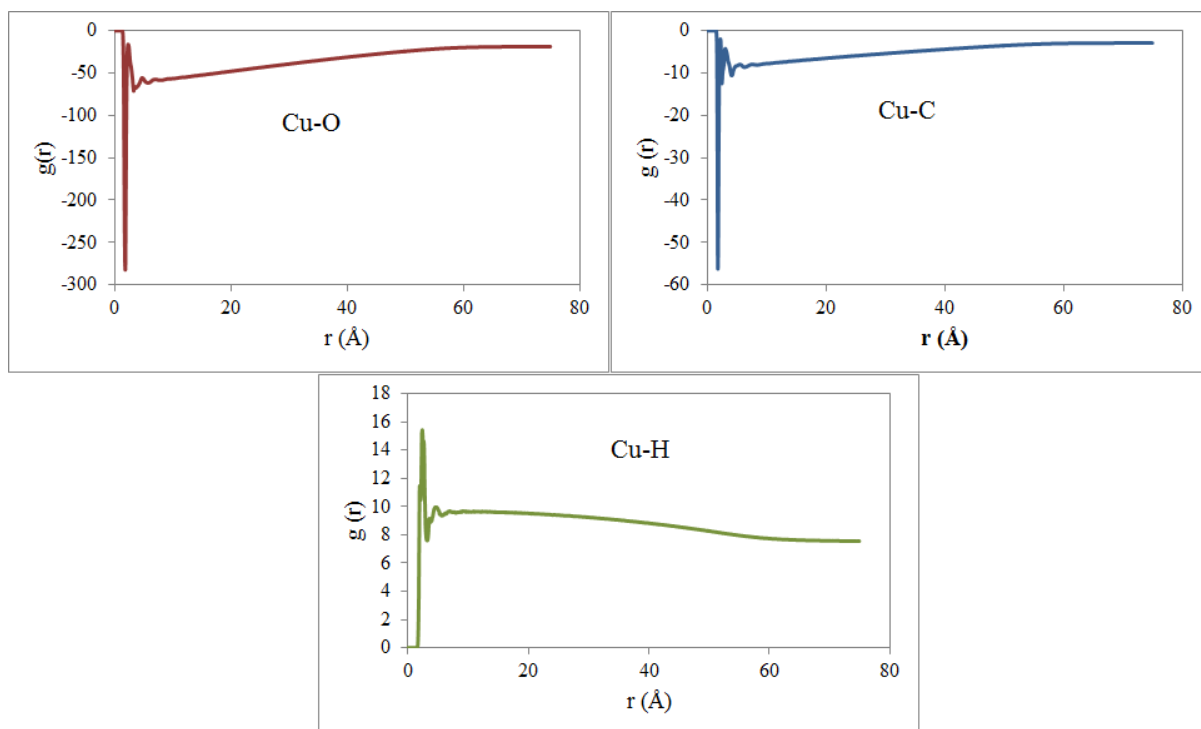
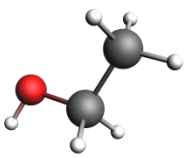
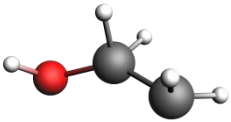

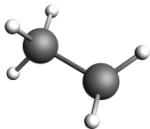
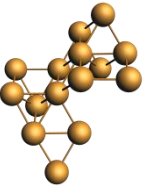
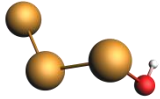
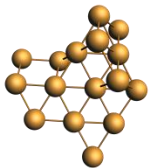
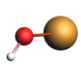
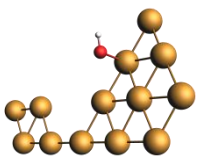
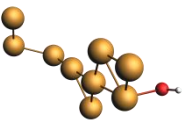
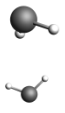
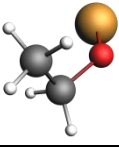
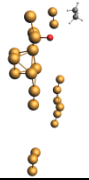
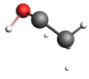
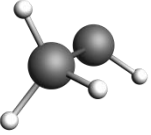

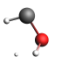
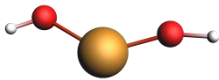
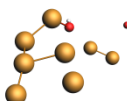
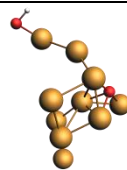
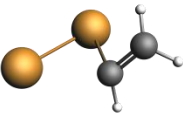
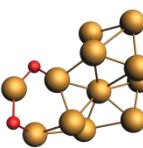
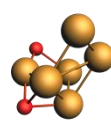
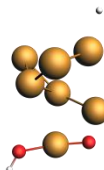
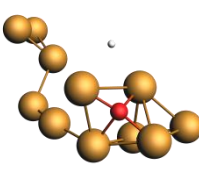
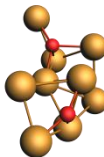


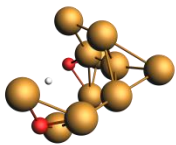
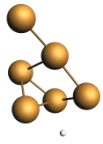
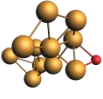
Fig. S12. Radial distribution function of copper atoms bound with oxygen, carbon, and hydrogen showing the amorphous structure of the Cu sphere after simulation of the MB1 model due to rapid cooling. Our goal here is to study bond breaking and bond formation during heating of the spheres in the ethanol bath; therefore, the cooling regime and formation of the crystalline structure were not studied. Reducing the cooling rate to study crystallization is an extremely time-consuming process in RBMD simulations of such large models, which are investigated in this study.

Table S13. Timeline of new species formed during molecular dynamics simulation of the MB7 model. These compounds were selected among hundreds of new species according to their higher participation in reactions at different time steps. We presented these molecules to show the accurate oxidation evolution during the heating of the Cu-ethanol model. The mechanism steps of (I) ethanol absorption, (II) hydroxyl cleavage, (III) Cu cluster formation, (IV) ethanol dissociation, (V) surface oxidation, and (VI) net oxidation were labeled for each new species.

Mechanism No.	Species	Description	Initial appearance (ps)	Species directly produced this	Species directly formed by this	Elementary reactions
I		ethanol	0	317	78	180
II		C ₂ H ₄ OH ⁻	25.33	35	16	10
II		H ⁺	25.33	790	23	342
IV		C ₂ H ₅ ⁺	25.66	369	74	199
III		Cu cluster	26	85	155	120
V		OH ⁻ absorption on Cu surface	26.33	698	67	328
III		Cu cluster	26.33	99	168	143

V		OH ⁻ absorption on Cu surface	26.33	796	42	351
V		OH ⁻ absorption on Cu cluster surface	26.66	155	60	77
V		OH ⁻ absorption on Cu cluster surface	29.66	331	83	175
IV		CH ₂	30.67	87	17	26
IV		C ₂ H ₅ O ⁻ absorption on Cu	32.33	140	36	61
V		Oxygen bonding on Cu cluster by breaking its bond with C ₂ H ₄	33.99	24	5	2
IV		Dehydrogenation of C ₂ H ₅ O ⁻	36.32	42	15	10
IV		C ₂ H ₄	36.65	144	32	59
IV		CH ₃	38.32	4	6	6
IV		CHOH+H	38.32	2	4	3

V		OH ⁻ absorption on Cu	40.65	333	100	198
V		Absorption of O ²⁻ on the surface of Cu cluster	69.62	64	27	15
VI		Bonding of oxygen with surrounding copper atoms	75.28	51	22	13
IV		Hydrocarbon-copper bonding	77.61	42	12	6
VI		Oxygen bonding in Cu cluster	83.94	10	11	2
VI		Oxygen bonding in Cu cluster	107.58	27	22	8
VI		Oxygen bonding in Cu cluster	161.19	24	9	2
VI		Hydrogen separation from bonding oxygen to Cu cluster	165.19	17	11	2
VI		Oxygen bonding in Cu cluster	219.47	5	8	2

VI		Hydrogen separation from bonding oxygen to Cu cluster	231.55	20	8	2
VI		Hydrogen separation from Cu cluster	242.22	3	15	2
VI		Oxygen bonding with surrounding copper atoms in Cu cluster	249.33	11	13	2

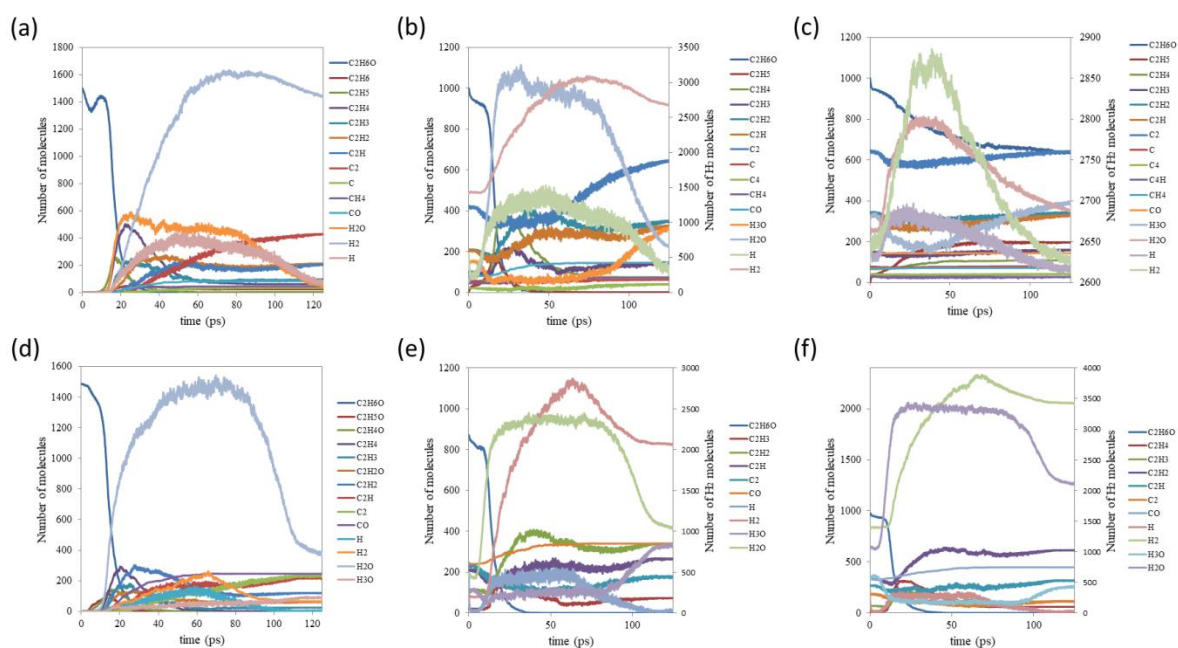


Fig. S13. Solvent analysis related to (a) the first stage, (b) the second stage, and (c) the third stage of MB10 model and (d) the first stage, (e) the second stage, and (f) the third stage of MB11 model. The increased formation of the reducing agents H₂, CO, and C₂ in the second and third rounds of thermal treatment shows greater dissociation of ethanol. The higher probability of reduction due to the increased formation of the above compounds is a reason for the formation of non-equilibrium kinetic byproducts, mainly on the surface of the spheres.

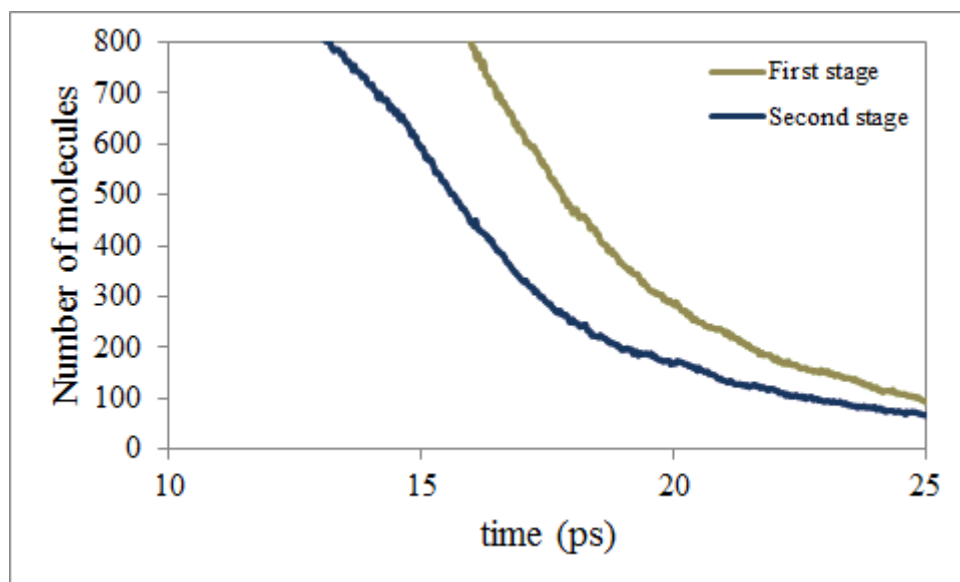


Fig. S14. The shift in the ethanol dissociation curve shows faster decomposition of the solvent in the second stage compared to the first stage in the MB10 model. Although the temperature of the simulation box is lower in the second stage, faster decomposition is achieved. According to the results of the MB1 and MB2 models, this shift is due to the net oxidation of the copper sphere in the previous stage.

f. DFT calculations

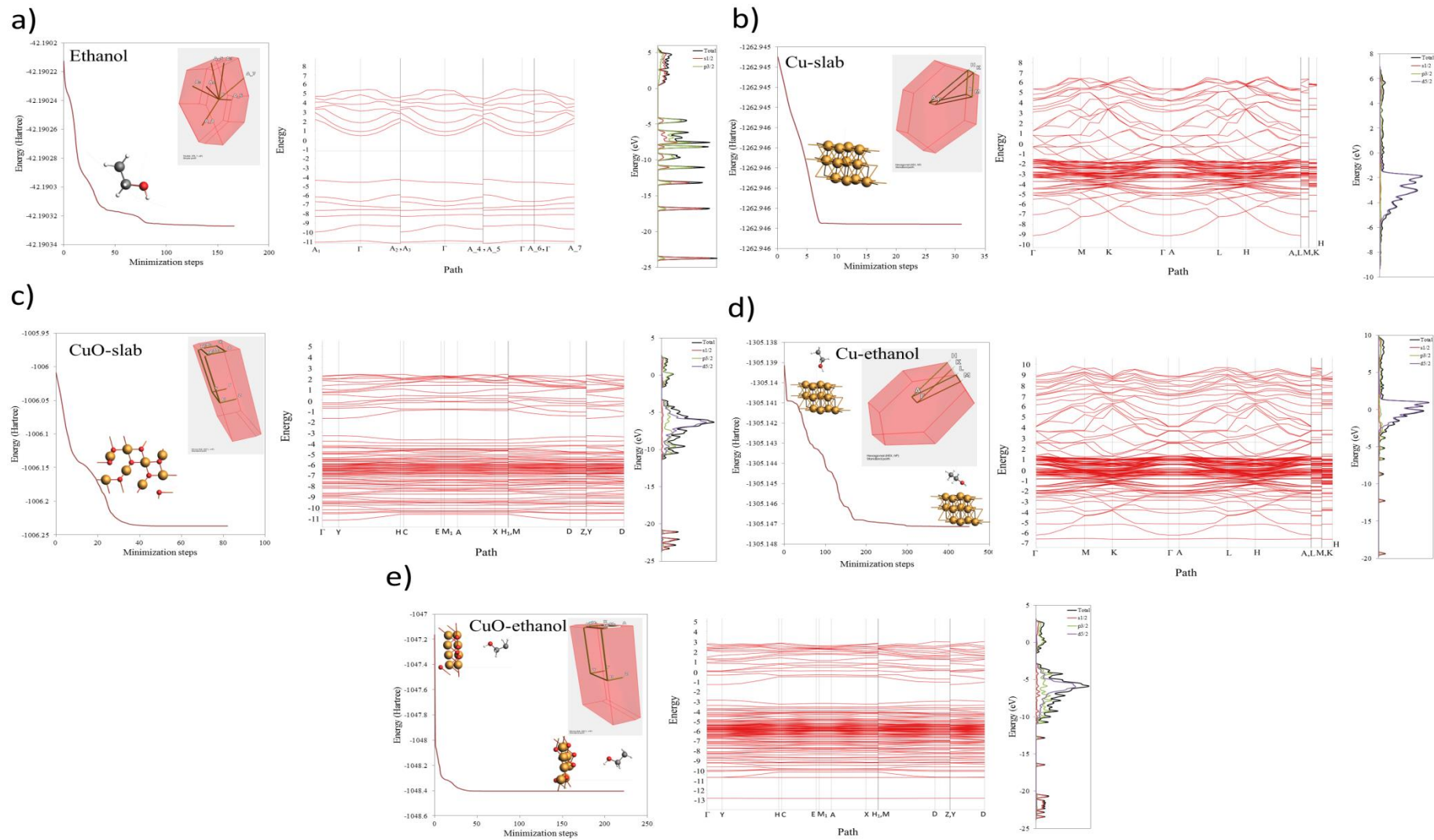


Fig. S15. DFT Models, structural relaxations, Brillouin zone K points, band structure, and density of states for (a) ethanol, (b) Cu-slab, (c) CuO-slab, (d) Cu- ethanol, and (e) CuO- ethanol. The calculated absorption energies of ethanol on the surfaces of Cu (111) and CuO (111) indicate that metallic copper is more willing to absorb ethanol by combining with both oxygen and hydrogen of the OH group due to its higher oxidation tendency. CuO, on the other hand, absorbs only the H atom of the OH group with a comparatively lower tendency. To ensure comparability of results, the same model size was chosen for both Cu and CuO. The band gap of CuO was calculated to be 1.45 eV, which is in good agreement with the experimental measurements of the previously published works. The density of states of ethanol does not affect the band gap of CuO and there is no state in the gap. On the other hand, the denser states of copper correspond to the density of states of ethanol; therefore, ethanol obviously affects the DOS of Cu.

Table S14. Minimized energy of structures and ethanol absorption energy on the (111) surface of Cu and CuO slabs

No.	compound	Minimized energy (Ry)	Absorption energy (eV)	
			Cu-ethanol	CuO-ethanol
1	Cu-ethanol	-2610.2942546099	-0.29448892467706	-
2	Cu-slab	-2525.8919558958		-
3	Ethanol	-84.3806541883		0.627013867946143
4	CuO-slab	-2012.4737593020	-	
5	CuO-ethanol	-2096.8083284431	-	

g. Raman spectra

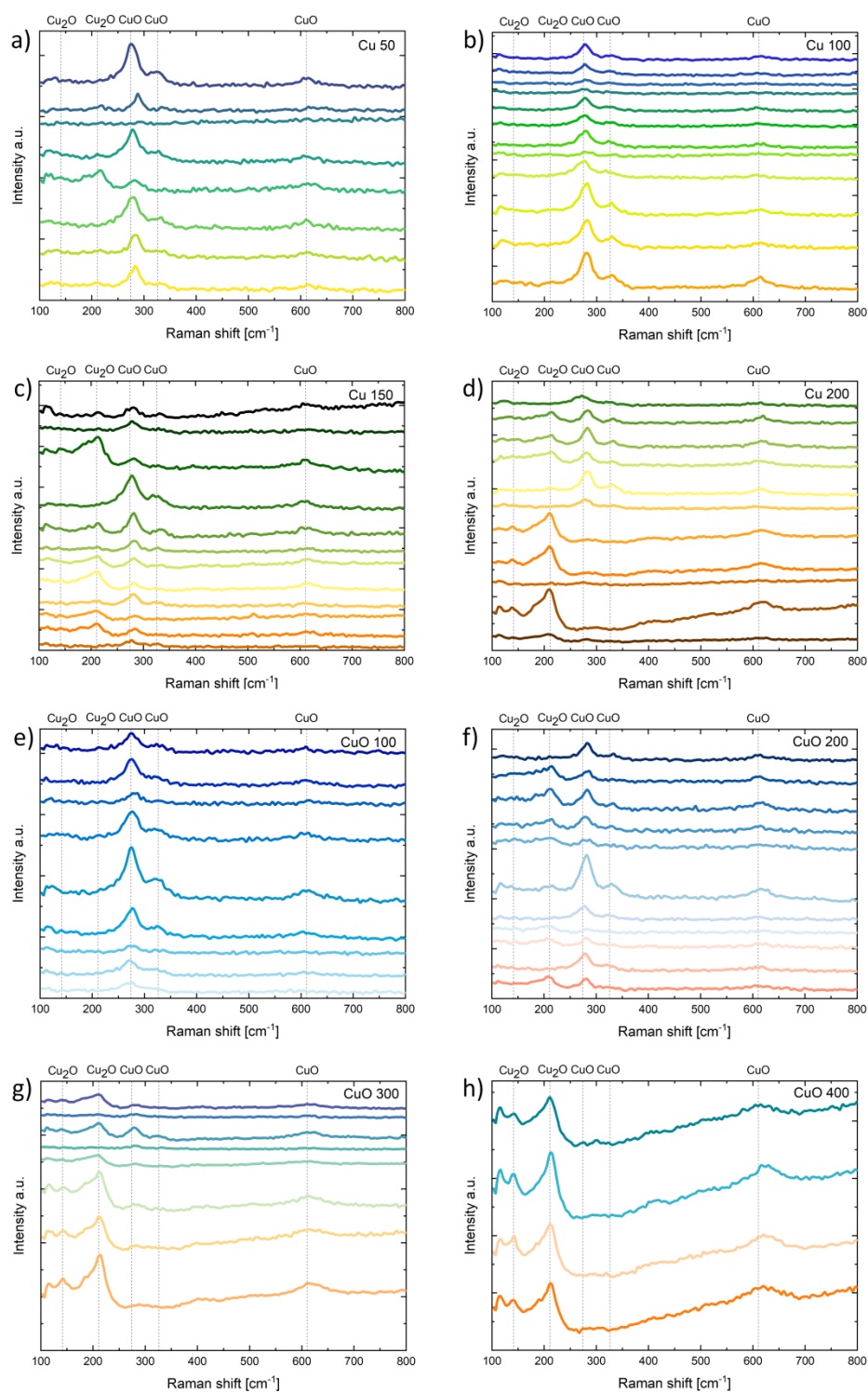


Fig. S16. Raman spectra of (a) Cu50, (b) Cu100, (c) Cu150, (d) Cu200, (e) CuO100, (f) CuO200, (g) CuO300, and (h) CuO400 samples with different focus of the laser spot. The differences between the absorptions of each sample are evident from the change in laser focus in the Raman spectra, illustrating the heterogeneous structure of the powder samples.

h. HRTEM analysis

We analyzed the particles of the CuO-ethanol group and found that the crystallized phases in each particle were consistent with the results of the D-J phase diagram (Fig. S22). For the particles that existed in dual-phase regions, at least the existence of one of the phases was confirmed. Table S17 shows the details of the particles highlighted in Fig. S22.

If we look in detail at the dependence of temperature and particle size, we can see that phase formation in submicron particles proceeds as follows. Nanoscale particles mostly crystallize in the Cu FCC structure. As the size increases, the preferred structure will be Cu₂O and for large particles, CuO. Higher laser fluence broadens the domains and shifts them toward the larger particles. Fast Fourier transform (FFT) analysis and calculation of the d-spacing using TEM images and SAED patterns of the different grains confirm our calculations (Fig. S23).

FFT analysis of HRTEM images shows that there is a possibility of coexistence of multiple phases, especially for larger particles with non-spherical shape. The reason for this is not only the crystallization in dual-phase regions, but also the different cooling rates in different directions of the non-spherical particles (Fig. S24).

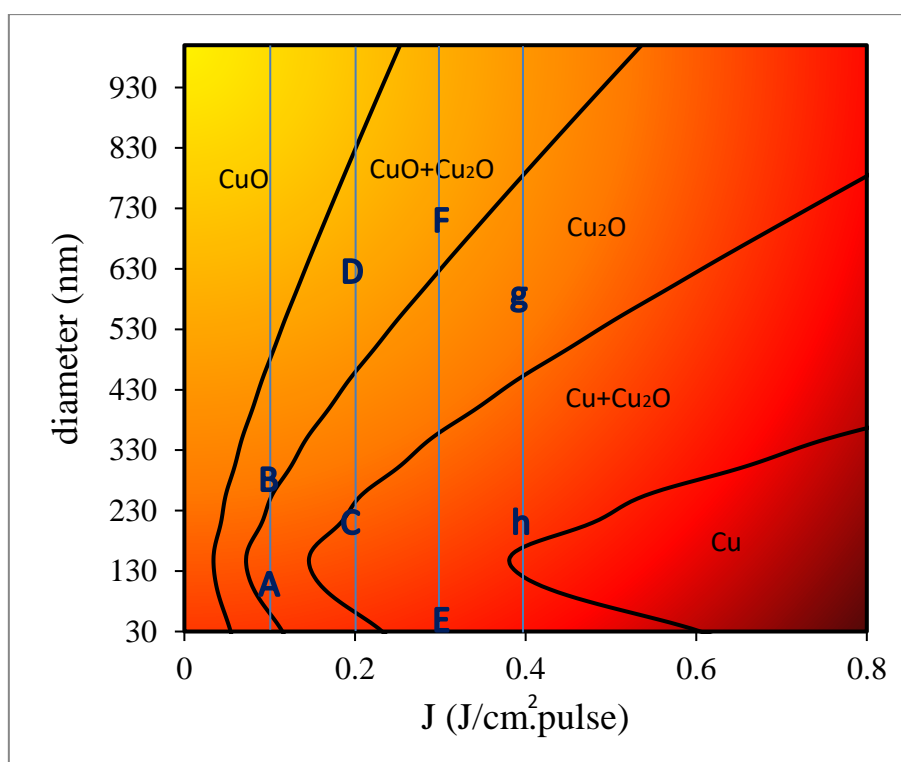


Fig. S17. D-J phase diagram for the PLIS process of CuO ethanol samples. The color gradient of the filling from dark red to yellow shows the decreasing temperature from the evaporation point to submelting.

Table S15. Phase recognition of the particles shown in the D-J phase diagram of Fig. S17

No.	index	Laser fluence (mJ/cm ² .pulse)	Size (nm)	Phase on the D-J diagram	Phase proved by HRTEM or SAED pattern
1	A	100	100	Cu ₂ O	Cu ₂ O
2	B	100	250	CuO+Cu ₂ O	CuO
3	C	200	150	Cu+Cu ₂ O	Cu ₂ O
4	D	200	620	CuO+Cu ₂ O	CuO+Cu ₂ O
5	E	300	15	Cu+Cu ₂ O	Cu
6	F	300	650	CuO+Cu ₂ O	CuO+Cu ₂ O
7	G	400	200	Cu+Cu ₂ O	Cu ₂ O
8	H	400	550	Cu ₂ O	Cu ₂ O

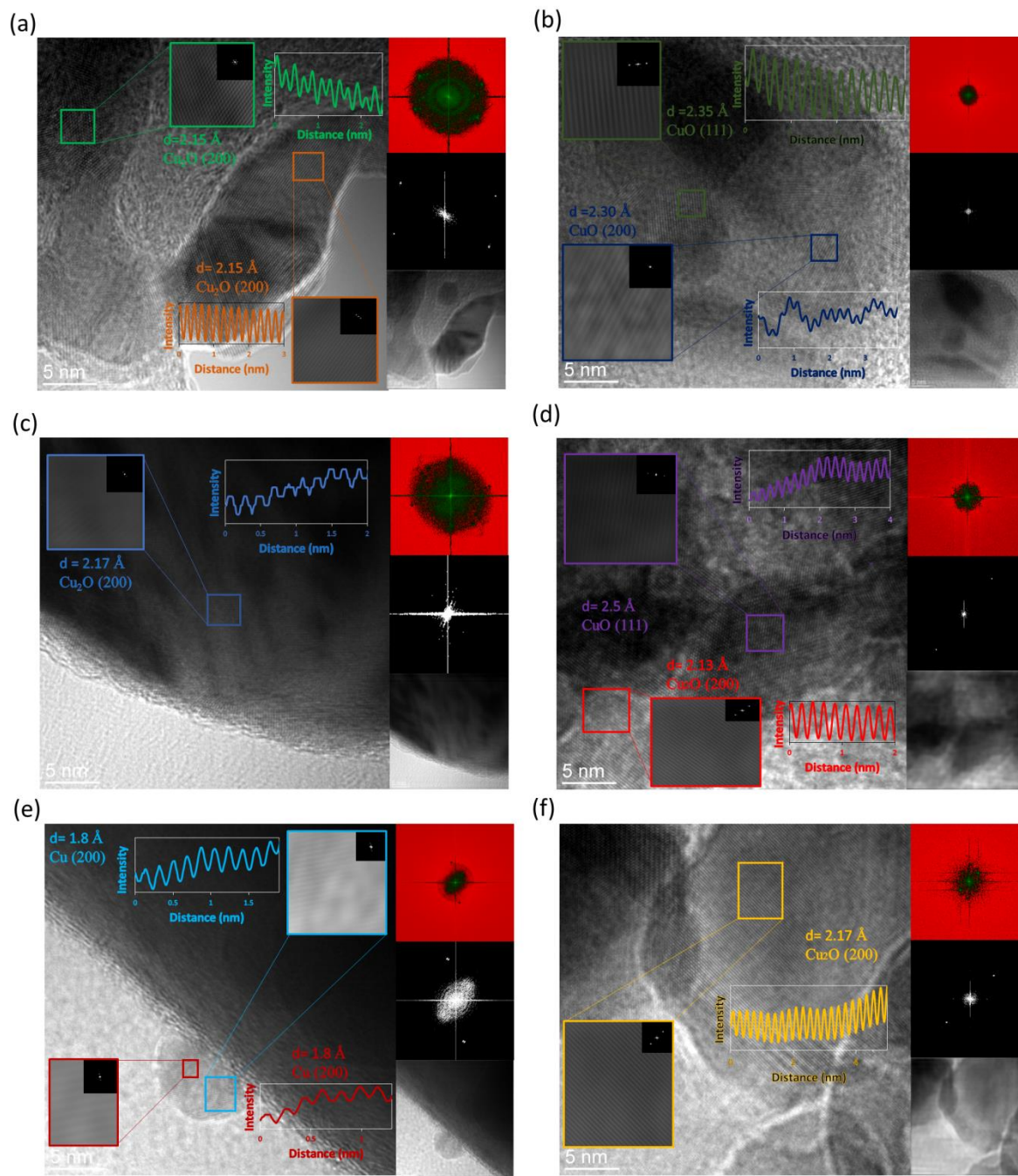


Fig. S18. The FFT analysis of the d-spacing of points (a) A, (b) B, (c) C, (d) D, (e) E, and (f) F in fig. S17.

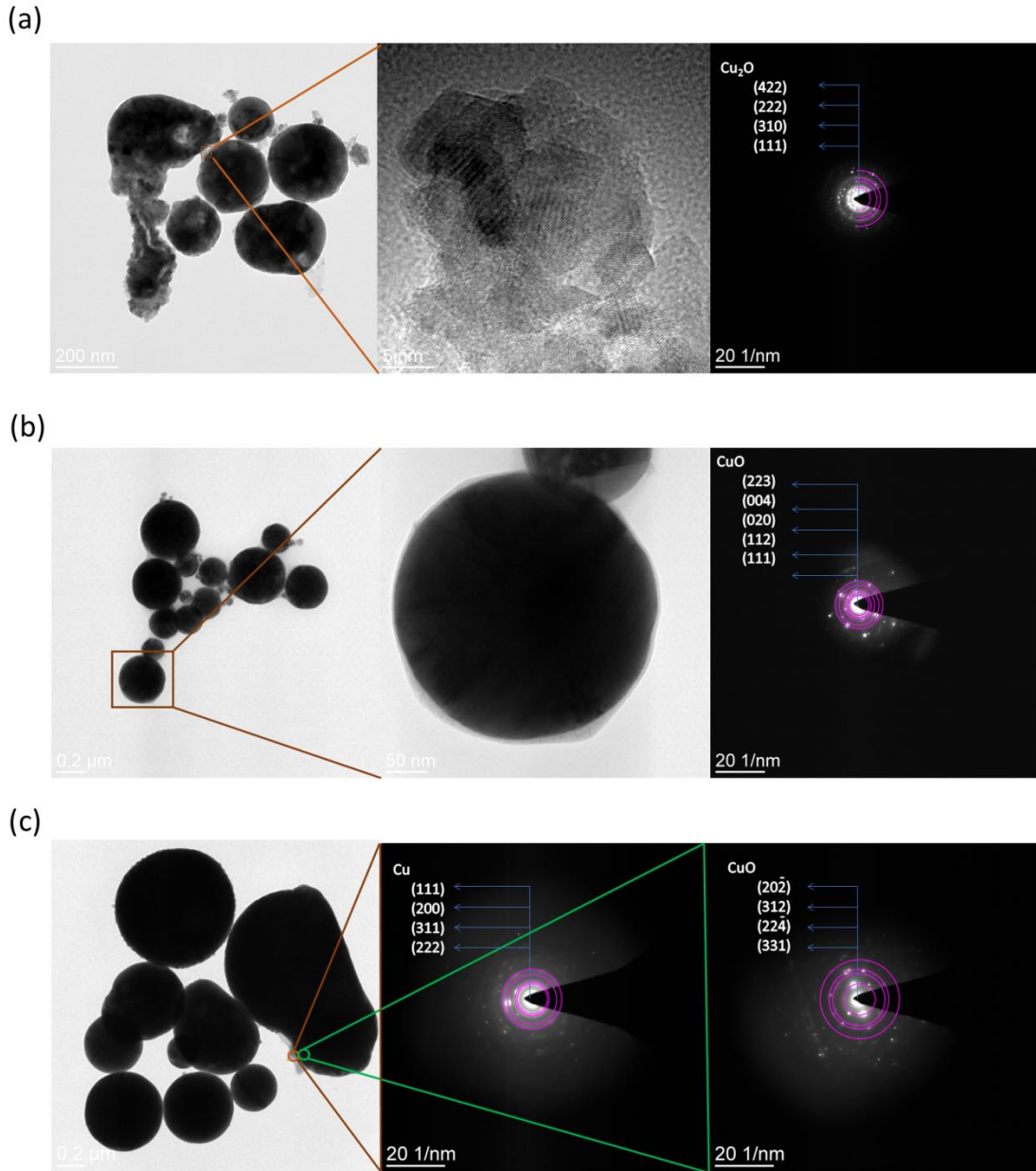


Fig. S19. TEM images and SAED patterns of (a) a 200 nm Cu_2O particle crystallized in a Cu50 sample, (b) a 350 nm CuO particle crystallized in a Cu100 sample, and (c) a 50 nm Cu particle on the surface of a 650 nm CuO particle in a Cu150 sample. The tendency of the small particles to crystallize in the Cu structure and the large particles to crystallize in the copper (I) and (II) phases is consistent with the J-D and T-D curves.

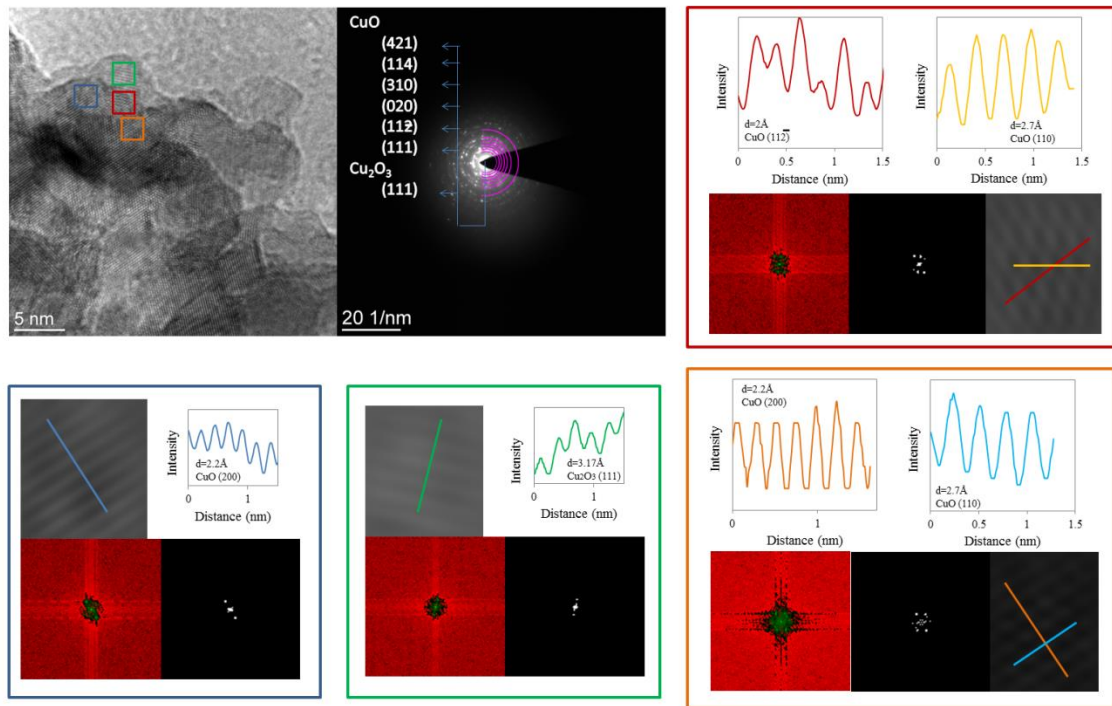


Fig. S20. FFT analysis of the different phases crystallized on the surface of a particle after the PLIS process of the Cu50 sample. The accumulation of oxygen on the surface or at the interface between the CuO and Cu₂O phases is the reason for the crystallization of Cu₂O₃, which can be seen in this figure.

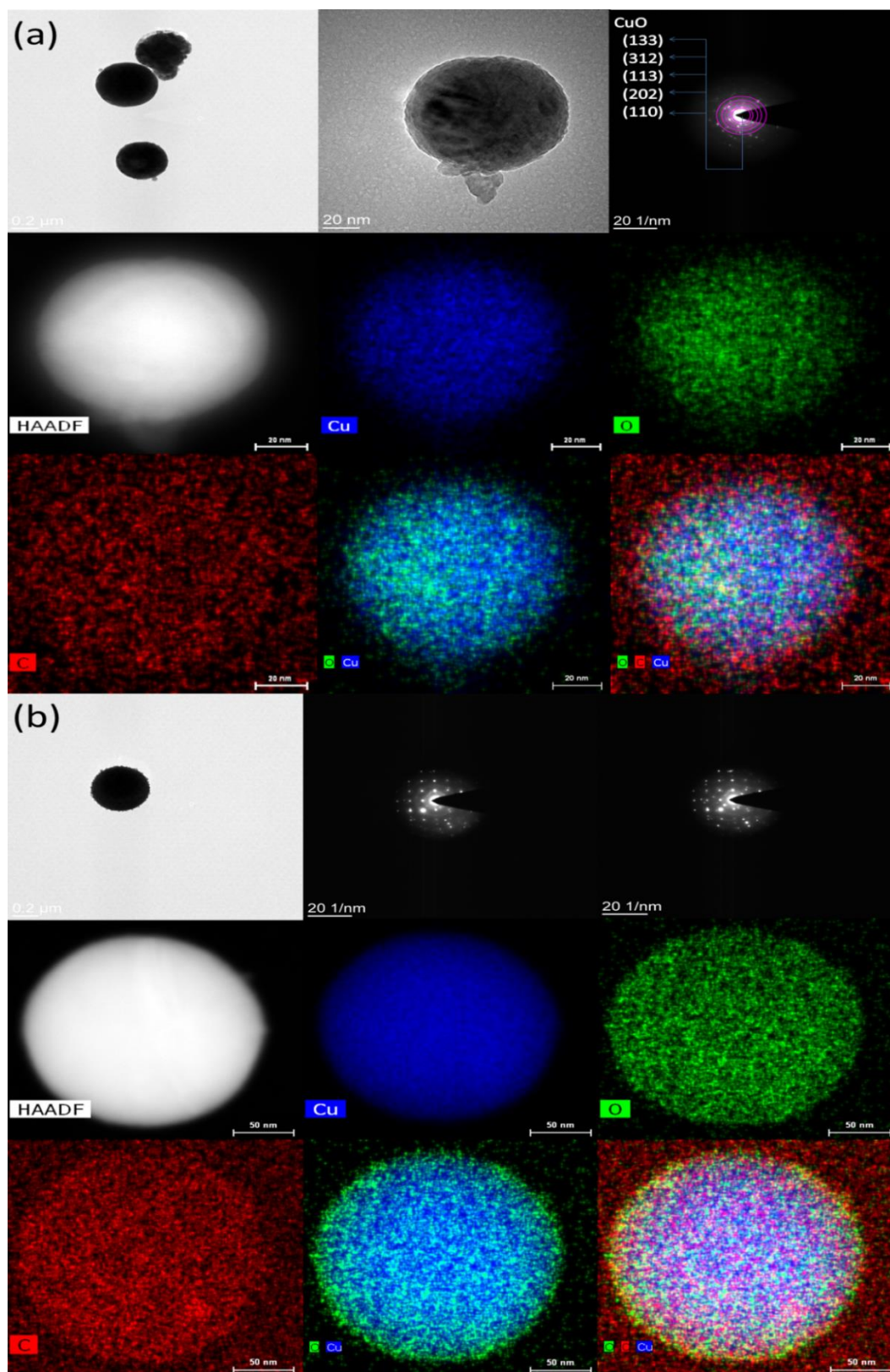


Fig. S21. EDX-HAADF Elemental map of particles formed in (a) CuO100 and (b) CuO300 samples. The enrichment of oxygen on the surface of the spheres, which is the reason for the formation of non-equilibrium phases, is obvious.

i. Zeta potential and particle size distribution

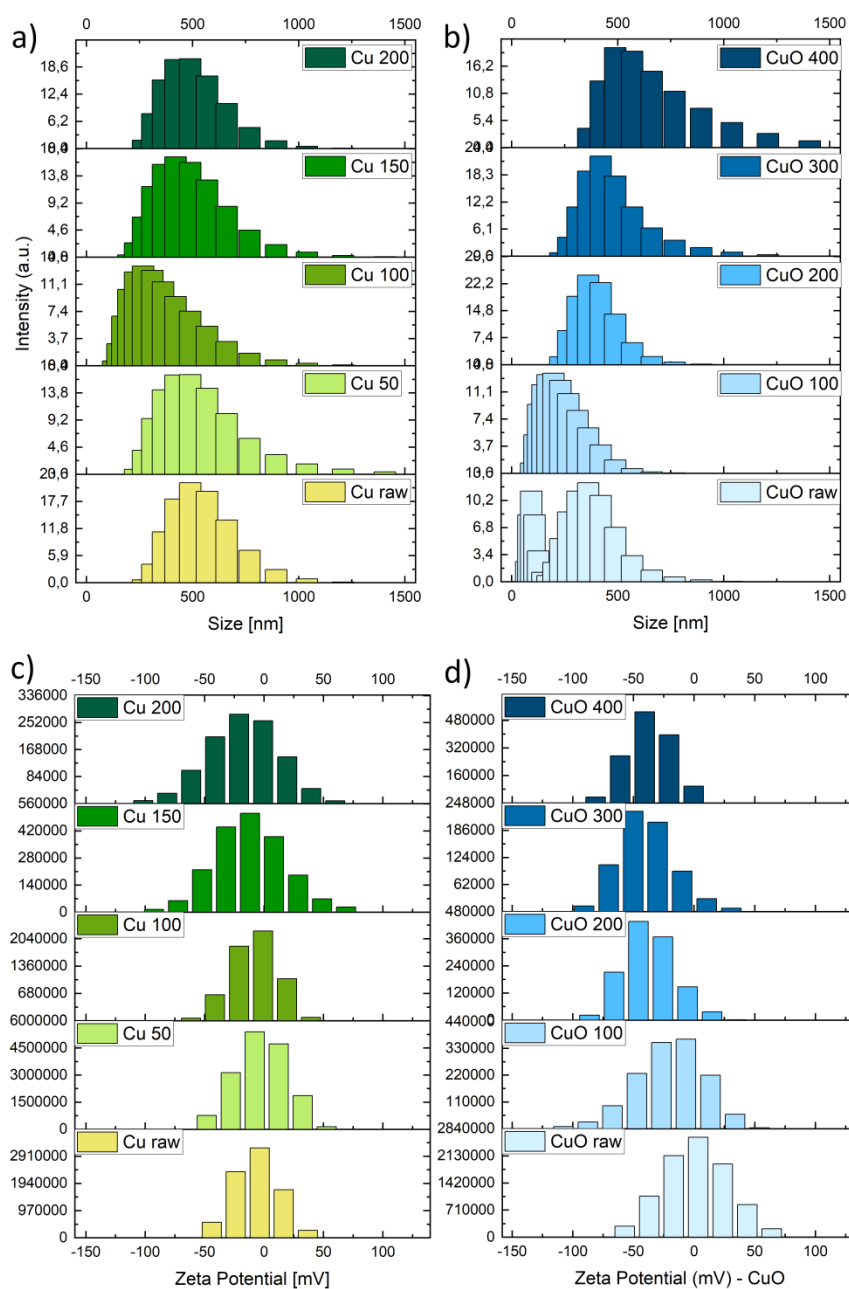


Fig. S22. DLS particle size distribution of agglomerates resulted from the PLIS process of (a) Cu-ethanol and (b) CuO-ethanol samples. Zeta potential of (c) Cu-ethanol and (d) CuO-ethanol suspensions. There is a relationship between Zeta potential and the size distribution of the agglomerates [7]. Thus, by changing the zeta potential, we can control the size of the final particles resulting from PLIS (see also supplementary part i).

j. Mathematical modeling of particle growth during the PLIS process

j.1. Categorization of suspensions

In the pulsed laser irradiation of suspensions (PLIS) method, a specific volume of a suspension is irradiated with a pulsed laser. The unfocused laser pulse has a constant cross section through which a volume fraction of the suspension is probed in each pulse [1-10]. Here we define η as the volume fraction of the suspension probed by a laser pulse, which is constant throughout the process. It is calculated from the ratio of the volume of the suspension probed by a laser pulse (V_L) and the volume of the suspension (V_s), as shown schematically in Fig. S23.

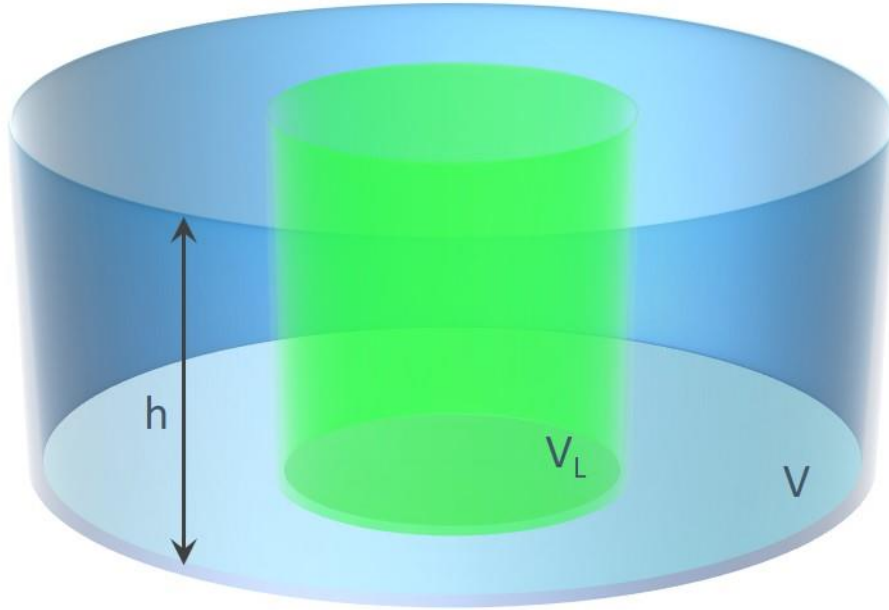


Fig. S23. Visualization of a laser beam through a container containing a suspension

If the container has a cylindrical shape, the height of both cylinders is the same, then

$$\eta = \frac{V_L}{V_s} = \frac{\pi r_L^2 h}{\pi r_s^2 h} = \left(\frac{r_L}{r_s}\right)^2 \quad (\text{S1})$$

If we know the particle sizes and/or the distribution of agglomerates in the suspension, the total number of spherical particles in a suspension (n_T) is calculated by the ratio between the weight of the solid added to the solvent (m_T) and the weight of the spherical particles (m_p).

$$n_T = \frac{m_T}{m_p} = \frac{3m_T}{4\rho\pi r_p^3} \quad (\text{S2})$$

where, ρ is the density of the solid phase and r_p is the radius of the particles. The maximum number of spheres that can be probed by a laser pulse n_L is calculated by the ratio of the laser cross section (A_L) to the surface area of the particle (A_p).

$$n_L = \frac{A_L}{A_p} = \frac{4\pi r_L^2}{4\pi r_p^2} = \left(\frac{r_L}{r_p}\right)^2 \quad (\text{S3})$$

Here, r_L and r_p are radii of the laser pulse and spherical particles, respectively. As for n_L , it could be called the probe limit. It means that it is impossible to probe more than n_L in each laser pulse. Using

the above equations, let us divide the suspensions into two main categories with respect to the PLIS process.

$$\begin{cases} n_T \eta < n_L \rightarrow \text{dilute suspension} \\ n_T \eta > n_L \rightarrow \text{dense suspension} \end{cases} \quad (\text{S4})$$

As shown, dense and dilute suspensions are those in which the concentration of the solid phase is above and below the probe limit, respectively. Fig. S24 shows the schematic diagram of the particle probe showing both dense and dilute suspensions.

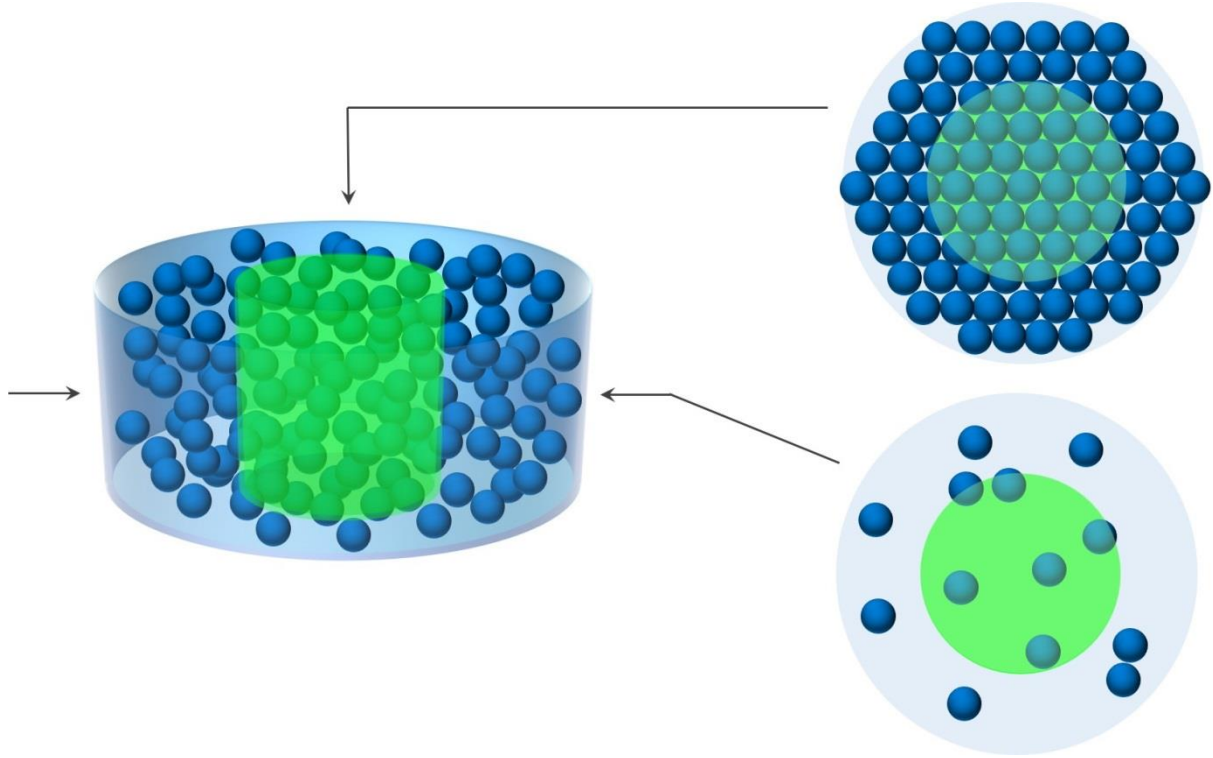


Fig. S24. Schematic representation of the particle probe in dense and dilute suspensions

j.2. Probability of the probe

Suppose a suspension is irradiated with laser pulses of frequency ν for t seconds. The probability of the probe (X) for a dense suspension can be calculated as follows,

$$X = P\nu t \quad (\text{S5})$$

In this equation, P is the fraction of particles probed during a laser pulse, formulated by,

$$P = \frac{N_L}{N_T} = \frac{\left(\frac{r_L}{r_p}\right)^2}{\frac{3m_T}{4\rho\pi r_p^3}} = \left(\frac{4\rho\pi r_L^2}{3m_T}\right) r_p = A r_p \quad (\text{S6})$$

Here A is the cyclic wavenumber constant (repetition number) with the unit (1/cm) depending on the properties of the suspension and the laser pulse.

$$A = \frac{4\rho\pi r_L^2}{3m_T} \quad (\text{S7})$$

Using Eq. (S6), Eq. (S5) is rearranged to be,

$$X = A r_p \nu t \quad (\text{S8})$$

On the other hand, the probability of the probe (X) for a dilute suspension is independent of the concentration of the powder and is defined as,

$$X = \eta vt \quad (\text{S9})$$

Probability of the probe (X) can vary from zero to larger amounts. It can also be divided into two ranges.

$$\begin{cases} 0 < X < 1 \rightarrow \text{partial probe} \\ X > 1 \rightarrow \text{complete probe} \end{cases} \quad (\text{S10})$$

A number less than one means that only a portion of the spheres were probed with the pulsed laser; thus, there still would be raw material in suspension. On the other hand, a number greater than one means that all particles have been irradiated at least once with the pulsed laser; thus, there is no remaining initial phase after irradiation. In the case of the partial probe, the amount of remaining raw material (R) is calculated as follows,

$$R = (1 - X) \times 100 \quad (\text{S11})$$

According to the above equations, the minimum time required for irradiation of all particles in the suspension is

$$\begin{cases} t = 1/\eta v \rightarrow \text{dillute suspension} \\ t = 1/pv \rightarrow \text{dense suspension} \end{cases} \quad (\text{S12})$$

As mentioned earlier, the probability of a probe does not depend on the particle size in dilute suspensions, but it is a function of the size of the particles in a dense suspension, as formulated in Eq. (S8). Since X and r_p depend on each other and change with time, particle growth must be parameterized during the PLIS process.

j.3. Particle growth without phase transition

Agglomerates consist of several particles connected by weak forces. The laser pulse melts the components of the agglomerates and joins them together to form larger particles. Imagine that there are n identical spheres of radius r_{p_0} that combine to form a larger sphere (r_p). In this case the resulting radius of the sphere is [S9],

$$r_p = \sqrt[3]{n} r_{p_0} \quad (\text{S13})$$

Here, n is the number of particles forming the agglomerate as shown in Fig. S25.

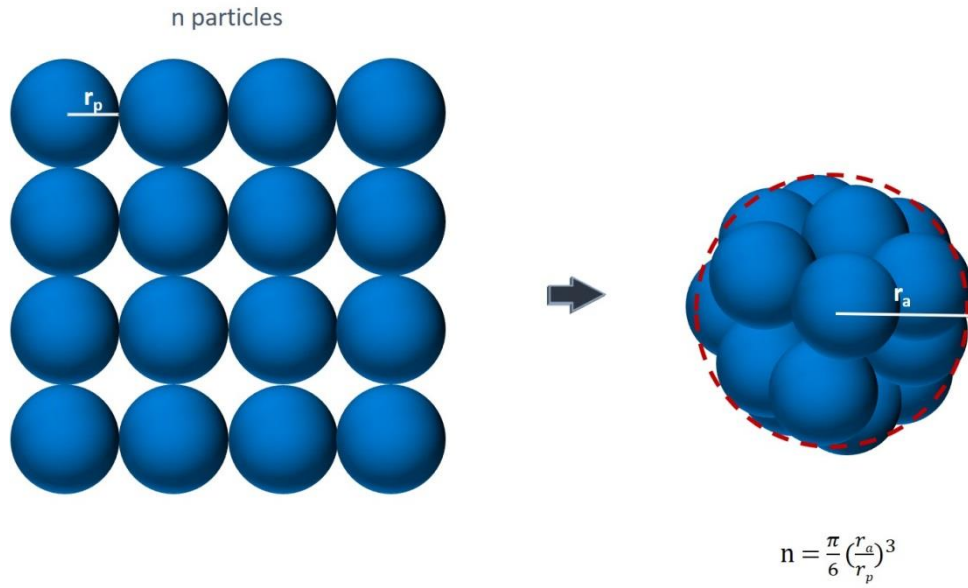


Fig. S25. Visualization of the sphere packing (n)

If the radius of particle and agglomerate is respectively r_p and r_a , then

$$n = \frac{\pi}{6} \left(\frac{r_a}{r_p} \right)^3 \quad (\text{S14})$$

During the PLIS process, the average number of probes of the agglomerates is equal to the probability of the probe (X); therefore, the radius of the final particles (Fig. S26) is,

$$r_p = (\sqrt[3]{n})^X r_{p_0} \quad (\text{S15})$$

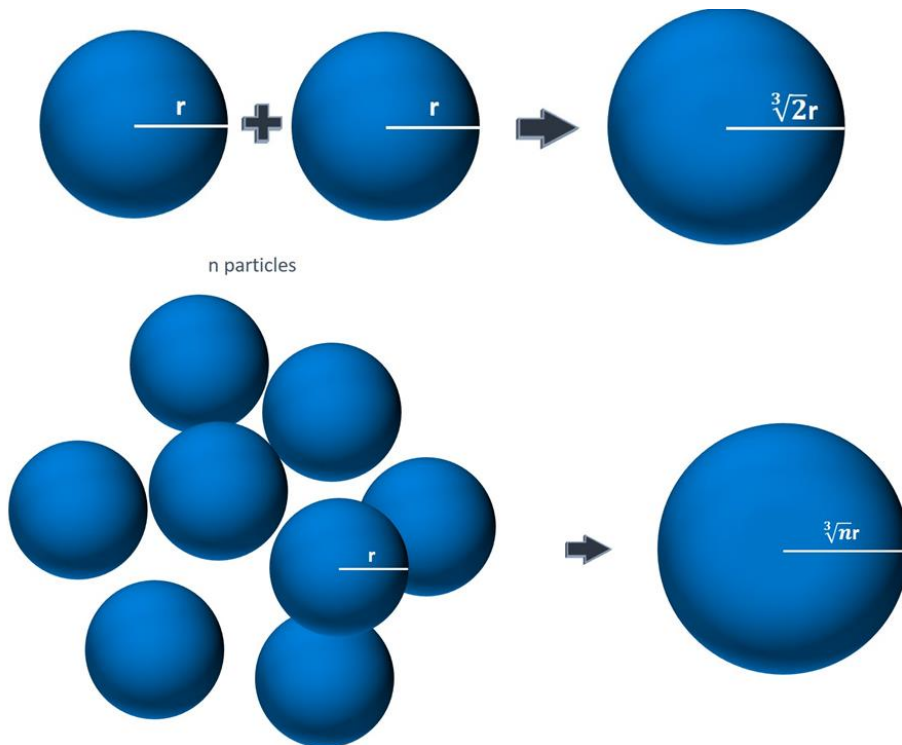


Fig. S26. Size change during the particle merging

And then X would be,

$$X = 3 \log_n \left(\frac{r_{pX}}{r_{p0}} \right) \quad (\text{S16})$$

Fig. S26 shows the schematic representation of particle merging during the PLIS process. Based on the zeta potential and the weight of the agglomerates, we know that there is an inverse relationship between the size of the particles (r_p) and the number of particles forming the agglomerate (n). When n decreases by the ratio of particle growth,

$$n = n_0 \frac{r_{p0}}{r_p} \quad (\text{S17})$$

Then, the radius of the particle after X irradiation cycles is,

$$r_p = r_{p0} \left(\frac{n_0 r_{p0}}{r_p} \right)^{X/3} \quad (\text{S18})$$

Fig. S27 shows the schematic visualization of the variations of factor n during the PLIS process. By simultaneously solving Eq. (S8) and Eq. (S18), the quantities X and r_p could be calculated throughout the PLIS process.

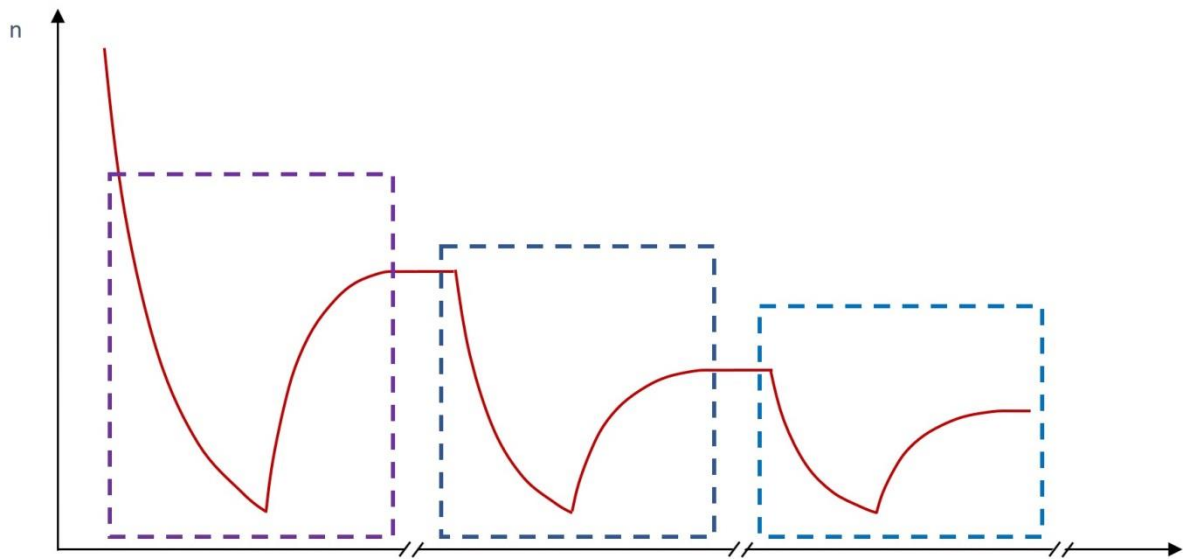


Fig. S27. Schematic representation of the variation of the factor n during the PLIS process

If we consider,

$$\frac{r_p}{r_{p0}} = y \quad (\text{S19})$$

Then,

$$y = \left(\sqrt[X+3]{n_0} \right)^X \quad (\text{S20})$$

A mathematical transformation changes the form of Eq. (S20) to,

$$X \ln n_0 = (X + 3) \ln y \quad (\text{S21})$$

j.4. Particle growth with phase transition

As mentioned earlier, during the PLIS process, the average probe is equal to the probability of the probe (X); if phase transitions occur during each probe, then the radius of the final particles is also proportional to the ratio of the initial (ρ_0) and final (ρ_1) phase densities. Here we define a parameter S , which is the ratio between the initial phase and the resulting phase, as,

$$S = \frac{\rho_0}{\rho_r} \quad (\text{S22})$$

By applying Eq. (S22), Eq. (S15) changes to

$$r_p = S(\sqrt[3]{n})^X r_{p_0} \quad (\text{S23})$$

Substituting Eq. (S17) and Eq. (S19), yields the new form of Eq. (S22) as,

$$y = S\left(\frac{n_0}{y}\right)^{X/3} \quad (\text{S24})$$

And by a mathematical transformation,

$$\left(\frac{X+3}{3}\right) \ln y = \ln S + \frac{X}{3} \ln n_0 \quad (\text{S25})$$

In the case of the present study, copper oxidizes in different states depending on the temperature of the sphere; therefore, Eq. (S25) is used for the calculations.

j.5. Agglomerate distribution effect

The above equations can be solved for mono-disperse agglomerates or for agglomerates that change in a range. In suspensions, the sizes of agglomerates usually conform to the Gaussian distribution. Therefore, the resulting size distribution can be calculated numerically or using the Gaussian distribution model adapted for a case study.

j.6. Application of model for the current study

Using the data in Table S16, we calculated how X changes with particle/agglomerate size for the Cu-ethanol and CuO-ethanol samples (using Eq. S8), as shown in Fig. 4i. If the particles were dispersed without agglomeration, 37% of the Cu and 26% of the CuO would be probed after 1 hour of irradiation. For Cu agglomerates with a radius greater than 80 nm and CuO agglomerates with a radius greater than 110 nm, the value of X reaches one. Considering the average size of the agglomerates in the Cu-ethanol and CuO-ethanol suspensions, the particles are irradiated more than once; therefore, there is no residual phase in the samples.

Table S16. Laser and suspension parameters for the calculation of the X factor

No.	Parameter	Cu-ethanol	CuO-ethanol
1	Concentration of solid phase (gr/lit)	0.0027	
	Weight of solid phase (gr)	0.027	
2	Particle size	30	40
3	Density (gr/cm ³)	8.96	6.3
4	Laser repetition (Hz)	10 Hz	
5	Laser cross section (cm)	0.07 cm	
6	Irradiation time (hr)	1	
7	Mean size of Cu agglomerates (nm)	300	350
	n_0	523.33	350.60

The n_0 value for the average size of agglomerates is shown in Table S16. Using the n_0 value and Eq. (S20), $y - X$ curves were calculated (Fig. 4j). Using Eq. (S19), these curves show how the agglomerates grow in both Cu-ethanol and CuO-ethanol suspension systems. Table S17 shows the maximum size of the sphere that can be melted by a laser pulse, the size of the final agglomerate measured by DLS, the mean size of the particles measured on the images from SEM, and the probability of probe (X) for all samples.

Table S17. Amounts for maximum size of particles that can be melted, average size of final agglomerates, average size of particles, and probability of probe

Sample code	Maximum size of particle that can be melted	Average size of resulted agglomerates	Average size of particles	X			
				Without phase transition	With Cu » CuO transition	With Cu » Cu ₂ O transition	With CuO » Cu ₂ O transition
Cu50	250	450	250	1.54	1.28	1.25	-
Cu100	400	320	313	1.80	1.53	1.50	-
Cu150	550	400	390	2.11	1.83	1.79	-
Cu200	700	500	470	2.35	2.05	2.00	-
CuO100	250	400	392	1.92	-	-	1.87
CuO200	450	550	534	2.38	-	-	2.33
CuO300	600	680	559	2.47	-	-	2.42
CuO400	750	820	734	2.97	-	-	2.92

According to the results of Table S17, the agglomerates are irradiated at least once and at most 3 times. The difference between the average size of the agglomerates and the particles for the particles obtained from the Cu50 sample is due to the small size of the particles and their tendency to agglomerate more. The difference between the maximum size of the melted particles and the average size of the agglomerates is due to the fact that more than 1 hour of irradiation at higher laser fluence is required for these two parameters to have the same value.

k. The role of laser-suspension parameters

We have tried to study all the important parameters related to the laser and the suspension in order to understand how the interaction between the laser and the matter takes place during PLIS. The following table briefly shows the role of effective parameters in PLIS.

Table 18. The role of parameters influencing the PLIS process

No.	Parameter			Explanation
	Category	Sub-category	Factor	
1	Laser	Beam	Fluence	The laser fluence affects the amount of energy absorbed by the particles according to their absorption efficiency, heat capacity and size
2		Pulse	Frequency	Laser frequency (laser repetitions) affects the probability of probe and particle growth, which is important for the final temperature of the particles
3			Shape	The pulse shape determines the development of the heating of particles
4			Duration	The pulse duration influences the heat dissipation and changes the heating trend of the particles
5	Suspension	Nano-particles	Absorption efficiency	The absorption efficiency is a function of the absorption cross section and the wavelength of the laser irradiation
6			Size of nano-particles	The size of the nanoparticles affects the number of particles that form the agglomerate (n), followed by the probability of probe
7		Solvent	Zeta potential	The zeta potential is influenced by the type of solvent, the type and size of the nanoparticles, and the preparation method, and affects the size distribution of the agglomerates
8			Size of agglomerates	The size of the agglomerates influences the probability of the probe and also the final temperature of the particles

1. Electrocatalysis behaviour

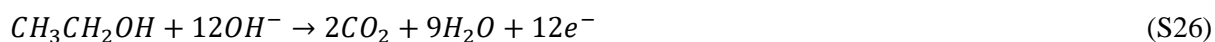
The electrochemical activity of the carbon supported Cu50/C, Cu100/C, Cu200/C, CuO100/C, CuO200/C, and CuO400/C catalysts was verified by CV, and their performance for EOR was investigated. The cyclic voltammograms for the catalysts were measured in 0.1 M NaOH (Fig. 6a). From these CV curves, the electrochemically active surface area (ECSA) was calculated using the hydrogen absorption region. The ECSA is a key parameter of fuel cell electrodes [33] that determines the mass activity of an analyzed catalyst [34]. Table S19 shows the highest value of ECSA (5065.00 $\text{cm}^2/\text{mg}_{\text{Cu}}$) for CuO200/C catalyst, while the smallest value is observed for CuO100/C (87.50 $\text{cm}^2/\text{mg}_{\text{Cu}}$). The highest ECSA values in CuO-ethanol samples are observed for Cu200/C (2037.50 $\text{cm}^2/\text{mg}_{\text{Cu}}$) and CuO400/C (2400.00 $\text{cm}^2/\text{mg}_{\text{Cu}}$) catalysts. A high ECSA value means that a large area of the electrode material is accessible to the electrolyte [35], which consequently should be considered as a high efficiency of ethanol oxidation (Fig. S28).

The highest and very similar catalytic property is observed for Cu100/C and Cu200/C catalysts. In general, Cu-ethanol/C catalysts have a higher potential in the ethanol oxidation reaction than CuO-ethanol/C catalysts (Figure 6b). This could be due to the consumption of part of the energy for the reduction of CuO to Cu [36]. In addition, the smallest similar values for the onset potential were also obtained for the Cu100/C and Cu200/C catalysts (Table S19). In accordance with the above results, in-situ FTIR studies were performed for Cu100/C and Cu200/C catalysts to show the final products of ethanol oxidation (Fig. 6b, c).

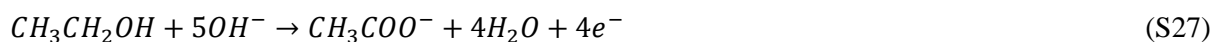
Peaks corresponding to CO_2 , CO, CH_3CHO and CH_3COOH [36, 37] located around 2360 cm^{-1} , 2100 cm^{-1} , 1340 cm^{-1} , and 1280 cm^{-1} are detected in the obtained IRRAS spectra (Fig. S29). Differences in the absorption of the peaks were studied to reveal changes in the amount of EOR products [S10-S13]. In the case of the Cu200/C catalyst, the absorbance of the peak corresponding to CO_2 oscillations increases to 0.25 during 3.5 hours and then decreases. For the peak CO, the absorbance increases up to 0.005, while the value of absorbance for CH_3CHO is stable at 0.045 during the whole EOR time. The highest absorption was visible for the CO_2 peak and the lowest for CO with a CO_2/CO ratio of about 43 (Figure 6b and Table S20).

For the Cu100/C catalyst, the absorbance of the CO_2 peak increases during the first 6 h and then remains between 0.55 and 0.75. A similar trend was observed for the peaks of CH_3CHO and CO. Finally, for CH_3COOH , the absorbance is stable at 0.003 for 11 hours and then increases dramatically to 0.016. The Cu100/C catalyst produces about 1400 times more CO_2 than CO and about 185 times more CH_3COOH . The Cu100/C catalyst produces about 4 times more CO_2 and CH_3CHO than the Cu200/C catalyst, which is a better choice as a catalyst (Table S21).

The hydroxyl group plays a crucial role in the mechanism of electro-oxidation of ethanol in alkaline media. When ethanol is completely oxidized to CO_2 in an alkaline direct fuel cell, 12 hydroxyl anions are consumed, giving up the same electrons [S14, S15].



In practice, ethanol is also partially oxidized to acetate in alkaline media, giving off a maximum of 4 electrons.



In composites, electro-oxidation occurs via both complete and partial mechanisms [S16, S17]; incidentally, the stronger formation of carbon dioxide compared to acetate confirms the dominant complete electro-oxidation mechanism in PLIS synthesized Cu-CuO-Cu₂O.

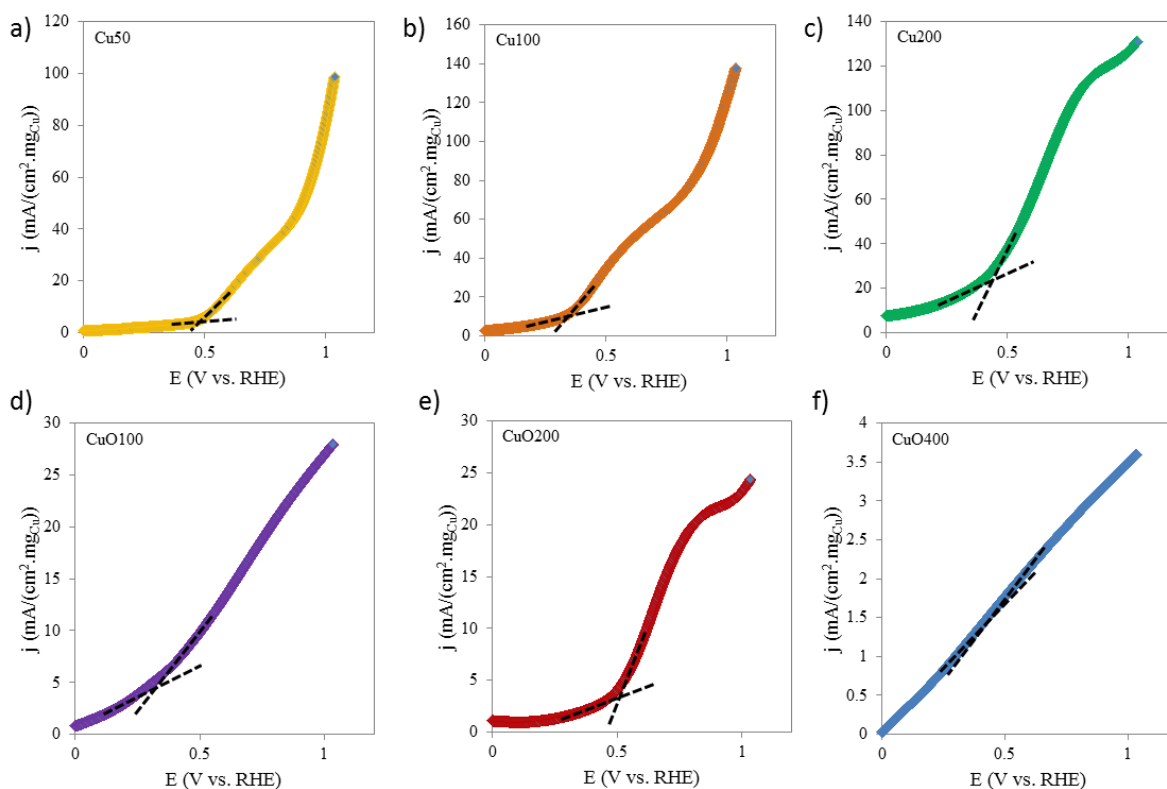


Fig. S28. Onset potential region for a: Cu50/C; b: Cu100/C; c: Cu200/C; d: CuO100/C; e: CuO200/C and f: CuO400/C. All curves were recorded in 0.1 M NaOH + 0.5 M C₂H₅OH solution at a scan rate of 50 mV/s at room temperature

Table S19. The ECSA and onset potential values for analyzed catalysts

Sample	ECSA (cm ²)	ECSA (cm ² /mgCu)	Onset potential z EOR (V)
Cu50	10.82	3381.25	0.49
Cu100	3.13	978.12	0.30
Cu200	6.52	2037.50	0.32
CuO100	0.35	87.50	0.20
CuO200	20.26	5065.00	0.34
CuO400	9.60	2400.00	0

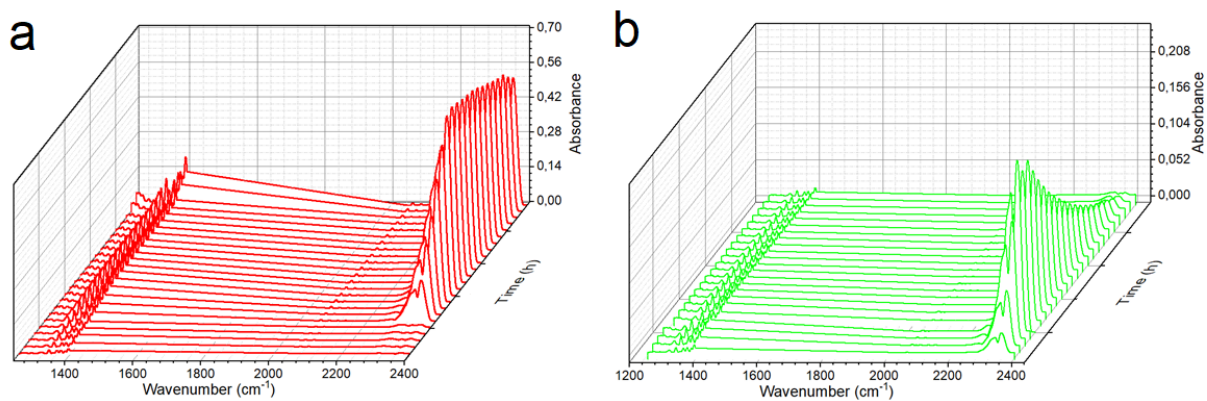


Fig. S29. In situ IRRAS spectra of (a) Cu100/C and (b) Cu200/C, each recorded after 30 min of measurement

Table S20. CO_2/CO , $\text{CO}_2/\text{CH}_3\text{CHO}$ and $\text{CO}_2/\text{CH}_3\text{COOH}$ ratios for Cu100 and Cu200 catalysts

Ratio	Cu200	Cu100
CO_2/CO	43.28	1432.92
$\text{CO}_2/\text{CH}_3\text{CHO}$	4.91	5.12
$\text{CO}_2/\text{CH}_3\text{COOH}$	3.37	184.73

Table S21. Ratio between Cu100 and Cu200 catalysts for the sum of absorption of CO_2 , CO , CH_3CHO and CH_3COOH

Substance	Cu100/Cu200 ratio
CO_2	4.04
CO	0.12
CH_3CHO	3.88
CH_3COOH	0.07

References

- [S1] V. Sudarsan. "Optical materials: fundamentals and applications." *Functional Materials: Preparation, Processing and Applications* (2012): 285-322.
- [S2] R. M. Waxler, and C. E. Weir. "Effect of pressure and temperature on the refractive indices of benzene, carbon tetrachloride, and water." *Journal of research of the National Bureau of Standards. Section A, Physics and chemistry* 67, no. 2 (1963): 163.
- [S3] Jan Jasny, Bernhard Nickel, and Pawel Borowicz. "Wavelength-and temperature-dependent measurement of refractive indices." *JOSA B* 21, no. 4 (2004): 729-738.
- [S4] Yurii V. Larichev, Boris L. Moroz, and Valerii I. Bukhtiyarov. "Electronic state of ruthenium deposited onto oxide supports: An XPS study taking into account the final state effects." *Applied surface science* 258, no. 4 (2011): 1541-1550.
- [S5] Kalina Grzelak, Maciej Trejda, and Jacek Gurgul. "Impact of Cerium Oxide on the State and Hydrogenation Activity of Ruthenium Species Incorporated on Mesocellular Foam Silica." *Materials* 15, no. 14 (2022): 4877.
- [S6] Julien Lam, and James F. Lutsko. "Solvent-mediated interactions between nanostructures: From water to Lennard-Jones liquid." *The Journal of Chemical Physics* 149, no. 13 (2018): 134703.
- [S7] Philipp Wagener, Jurij Jakobi, Christoph Rehbock, Venkata Sai Kiran Chakravadhanula, Claas Thede, Ulf Wiedwald, Mathias Bartsch, Lorenz Kienle, and Stephan Barcikowski. "Solvent-surface interactions control the phase structure in laser-generated iron-gold core-shell nanoparticles." *Scientific reports* 6, no. 1 (2016): 1-12.
- [S8] Valeria Orazi, Alfredo Juan, Estela Andrea Gonzalez, Jorge M. Marchetti, and Paula Verónica Jasen. "DFT study of ethanol adsorption on CaO (0 0 1) surface." *Applied Surface Science* 500 (2020): 144254.
- [S9] Mhand Hifi, and Rym M'hallah. "A literature review on circle and sphere packing problems: Models and methodologies." *Advances in Operations Research* 2009 (2009).
- [S10] L. Declan Burke, John A. Collins, and Maria A. Murphy. "Redox and electrocatalytic activity of copper in base at unusually low, premonolayer potentials." *Journal of Solid State Electrochemistry* 4, no. 1 (1999): 34-41.
- [S11] Evans A. Monyoncho, Tom K. Woo, and Elena A. Baranova. "Ethanol electrooxidation reaction in alkaline media for direct ethanol fuel cells." *Electrochemistry* 15 (2018): 1-57.
- [S12] Ken-ichiro Ota, Gerhard Kreysa, and Robert F. Savinell, eds. *Encyclopedia of applied electrochemistry*. New York: Springer, 2014.
- [S13] Hannes Frey, Arik Beck, Xing Huang, Jeroen Anton van Bokhoven, and Marc-Georg Willinger. "Dynamic interplay between metal nanoparticles and oxide support under redox conditions." *Science* 376, no. 6596 (2022): 982-987.
- [S14] Aya K. Buckley, Michelle Lee, Tao Cheng, Roman V. Kazantsev, David M. Larson, William A. Goddard III, F. Dean Toste, and Francesca M. Toma. "Electrocatalysis at organic-metal interfaces:

identification of structure–reactivity relationships for CO₂ reduction at modified Cu surfaces." *Journal of the American Chemical Society* 141, no. 18 (2019): 7355-7364.

[S15] Carsten Cremers, Dominik Bayer, Birgit Kintzel, Martin Joos, Florina Jung, Michael Krausa, and Jens Tübke. "Oxidation of alcohols in acidic and alkaline environments." *ecs transactions* 16, no. 2 (2008): 1263.

[S16] M. Li, A. Kowal, K. Sasaki, N. Marinkovic, D. Su, E. Korach, P. Liu, and R. R. Adzic. "Ethanol oxidation on the ternary Pt–Rh–SnO₂/C electrocatalysts with varied Pt: Rh: Sn ratios." *Electrochimica Acta* 55, no. 14 (2010): 4331-4338.

[S17] Manoj B. Gawande, Anandarup Goswami, François-Xavier Felpin, Tewodros Asefa, Xiaoxi Huang, Rafael Silva, Xiaoxin Zou, Radek Zboril, and Rajender S. Varma. "Cu and Cu-based nanoparticles: synthesis and applications in catalysis." *Chemical reviews* 116, no. 6 (2016): 3722-3811.